The thermal properties of porous andesite

Michael Heap, Alexandra R.L. Kushnir, Jérémie Vasseur, Fabian Wadsworth, Pauline Harlé, Patrick Baud, Ben Kennedy, Valentin Troll, Frances Deegan

The thermal properties of porous andesite

Michael J. Heap*[1], Alexandra R.L. Kushnir[1], Jérémie Vasseur[2], Fabian B. Wadsworth[3], Pauline Harlé[1], Patrick Baud[1], Ben M. Kennedy[4], Valentin R. Troll[5], and Frances M. Deegan[5]

[1]*Géophysique Expérimentale, Institut de Physique de Globe de Strasbourg (UMR 7516 CNRS, Université de Strasbourg/EOST), 5 rue René Descartes, 67084 Strasbourg cedex, France*

[2]*Earth and Environmental Sciences, Ludwig-Maximilians-Universität, Theresienstrasse 41, 80333 Munich, Germany*

[3]*Department of Earth Sciences, Science Labs, Durham University, Durham, DH1 3LE, U.K.*

[4]*Department of Geological Sciences, University of Canterbury, Private Bag 4800, Christchurch 8140, New Zealand*

[5]*Department of Earth Sciences, Section for Natural Resources and Sustainable Development (NRHU), Villavägen 16, Uppsala University, 752 36 Uppsala, Sweden*

Corresponding author: Michael Heap (heap@unistra.fr)

Abstract

The thermal properties of volcanic rocks are crucial to accurately model heat transfer in volcanoes and in geothermal systems located within volcanic deposits. Here we provide laboratory measurements of thermal conductivity and thermal diffusivity for variably porous andesites from Mt. Ruapehu (New Zealand) and variably altered basaltic-andesites from Merapi volcano (Indonesia) measured at ambient laboratory pressure and temperature using the transient hot-strip method. The specific heat capacity of each sample was then calculated using these measured values and the bulk sample density. Thermal conductivity and thermal diffusivity decrease as a function of increasing porosity, but specific heat capacity does not vary systematically with porosity. For a given porosity, saturation with water increases thermal conductivity and specific heat capacity, but decreases thermal diffusivity. Measurements on samples from Merapi volcano show that, compared to the unaltered samples from Mt. Ruapehu, hydrothermal alteration deceases thermal conductivity and thermal diffusivity, and increases specific heat capacity. We use an effective medium approach to parameterise these data, showing that when the porosity and pore-fluid properties are scaled for, the measured values agree well with theoretical predictions. We find that despite the microstructural complexity of the studied andesites, porosity is the principal parameter dictating their thermal properties. To understand whether the measured changes in thermal properties are sufficient to influence natural processes, we model heat transfer from magma to the surrounding host-rock by solving Fick's second law cast in 1D Cartesian (dyke geometry) and cylindrical (conduit geometry) coordinates. We provide models for different host-rock porosities (0-0.6), different initial magmatic temperatures (800-1200 °C), and different levels of host-rock alteration. Our modelling shows how the cooling of a

dyke and conduit is slowed by a higher host-rock porosity and by increased hydrothermal alteration. The thermal properties provided herein can help improve modelling designed to inform on volcanic and geothermal processes.

Keywords: Thermal conductivity; Thermal diffusivity; Specific heat capacity; Andesite; Porosity; Hydrothermal alteration

Highlights:

- Thermal conductivity decreases from 1.5 to 0.4 $W.m^{-1}.K^{-1}$ as porosity increases from 0.05 to 0.6.
- Thermal diffusivity decreases from 0.7-0.8 to 0.5-0.55 $mm^2.s^{-1}$ as porosity increases from 0.05 to 0.6.
- Specific heat capacity is 0.591-0.856 $kJ.kg^{-1}.K^{-1}$ and does not vary with porosity.
- Porosity plays a first-order role in dictating thermal properties.
- Cooling of a dyke/conduit is slowed by higher host-rock porosity and hydrothermal alteration.

1 Introduction

Volcanic systems are thermally dynamic environments (e.g., Oppenheimer et al., 1993; Harris et al., 1997; Harris and Stevenson, 1997; Wright et al., 2004; Hutchison et al., 2013; Heap et al., 2018). As a result, the thermal properties of volcanic rocks are an important input parameter for a wide range of predictive models. Examples include: the modelling of heat loss from lava flows, pyroclastic density current deposits, dykes, sills, conduits, and magma chambers (e.g., Irvine, 1970; Norton and Knight, 1977; Carrigan, 1984; Bruce and Huppert, 1989; Carrigan et al., 1992; Fialko and Rubin, 1999; Bagdassarov and Dingwell, 1994; Wooster et al., 1997; Annen et al., 2008; Nabelek et al., 2012; Heap et al., 2014; Schauroth et al., 2016; Heap et al., 2017a; Annen, 2017; Mattsson et al., 2018; Tsang et al., 2019), the modelling of the internal structure and hydrological system of volcanoes (e.g., Sammel et al., 1988; Ehara, 1992; Violette et al., 1996; Hurwitz et al., 2002, 2003; De Natale et al., 2004), ground deformation modelling (e.g., Del Negro et al., 2009; Currenti et al., 2010; Fournier and Chardot, 2012), outgassing models (e.g., Chiodini et al., 2001), models of viscous sintering (e.g., Wadsworth et al., 2014), and heat transfer in volcanic lightning storms (e.g., Wadsworth et al., 2017). In addition, the thermal properties of volcanic rocks are also of use in modelling designed to better understand large-scale fluid circulation, heat flow calculations, and temperature estimations at volcanic geothermal sites, such as those in Iceland (e.g., Bodvarsson et al., 1984; Flóvenz and Sæmundsson, 1993) and New Zealand (e.g., Mercer and Faust, 1979; Kühn and Stöfen, 2005). Finally, an understanding of the thermal properties of volcanic rocks is important due to their influence on permeability-enhancing thermal fracturing (e.g., Bauer and Handin, 1983; Siratovich et al., 2015; Lamur et al., 2018).

Due to the need for robust parameters for modelling, experimental studies have provided values of the thermal properties of volcanic rocks (e.g., Horai et al., 1970; Fuji and Osako, 1972; Robertson and Peck, 1974; Bagdassarov and Dingwell, 1994; Whittington et al., 2009; Romine et al., 2012; Mielke et al., 2015, 2016, 2017; Vélez et al., 2018; Hofmeister, 2019). Robertson and Peck (1974), for example, calculated the thermal conductivity of variably porous basalt from Hawai'i (USA) using the steady-state method. These authors found that thermal conductivity decreased from ~1.7 $W.m^{-1}.K^{-1}$ at a porosity <0.05 to ~0.2 $W.m^{-1}.K^{-1}$ at a porosity of ~0.85. Romine et al. (2012) found that the thermal diffusivity of rhyolite from Mono Craters (USA), measured using the laser-flash analysis method, decreased from ~0.65 to ~0.55 $mm^2.s^{-1}$ as temperature was increased from ~20 to ~430 °C, but remained constant from ~430 to ~1300 °C. These authors also calculated that the thermal conductivity of rhyolitic glasses and melts increases from ~1.1 to ~1.5 $W.m^{-1}.K^{-1}$ as temperature is increased from ~20 to ~1300 °C. Horai et al. (1970) and Fuji and Osako (1972) found that the thermal diffusivity of lunar basalt, measured using the modified Ångström method, decreased from ~0.7 to ~0.5 $mm^2.s^{-1}$ as temperature was increased from ~20 to ~230 °C. Mielke et al. (2015) measured the thermal properties of volcanic rocks (andesites and rhyolites) from the Tauhara geothermal field (New Zealand) using a portable device that measures thermal conductivity and thermal diffusivity using a modified optical scanning method. For example, they found average thermal conductivities of 1.32 and 1.11 $W.m^{-1}.K^{-1}$ for andesite lava (average porosity = 0.095) and rhyolite lava (average porosity = 0.275), respectively. Mielke et al. (2016) measured the thermal properties of volcanic rocks (andesite, dacite, and rhyolite) from the Taupō Volcanic Zone (New Zealand) using the optical scanning method. The thermal conductivities of the andesite (porosity = 0.023-0.130), dacite

(porosity = 0.108), and rhyolite (porosity = 0.231) samples were 1.19-1.70, 1.18, and 1.04 $W.m^{-1}.K^{-1}$, respectively. Despite these studies, there is a paucity of thermal property data (thermal conductivity, thermal diffusivity, and specific heat capacity) for volcanic rocks spanning a wide porosity range. These data are necessary to test effective medium expressions which, if found to well describe data for volcanic rocks, can be used in a variety of modelling approaches.

We report here on measurements of thermal conductivity, thermal diffusivity, and specific heat capacity for variably porous (porosity from 0.02 to 0.628) andesites from Mt. Ruapehu (Taupō Volcanic Zone); we additionally assess the role of water-saturation on the thermal properties of these andesite samples. Due to the ubiquity of hydrothermally altered zones at active volcanoes worldwide (e.g., Rosas-Carbajal et al., 2016; Byrdina et al., 2017; Heap et al., 2017b), we also investigated the influence of hydrothermal alteration on thermal properties by measuring a suite of variably altered basaltic-andesite samples from Merapi volcano (Indonesia). Theoretical predictions were then tested against these data. Finally, to understand whether the measured changes in thermal properties are sufficient to influence natural processes, we modelled the cooling of a dyke and a conduit by solving the heat equation in 1D in Cartesian and cylindrical coordinates, respectively. We provide models that cover a range of typical situations; namely, for different host-rock porosities (0, 0.3, and 0.6), different initial magmatic temperatures (800, 1000, and 1200 °C), and different alteration intensities.

2 Experimental materials and methods

Two suites of rocks were measured: (1) variably porous andesites from Mt. Ruapehu and (2) variably altered basaltic-andesites from Merapi volcano.

The andesites from Mt. Ruapehu (Taupō Volcanic Zone; see reviews by Graham et al., 1995; Wilson et al., 1995) were collected on the northern flank of the volcano (from the Whakapapa Formation; Hackett and Houghton, 1989). The blocks were collected thanks to a permit obtained through the Department of Conservation (DOC) and following consultation with the Māori Iwi. The andesites from Mt. Ruapehu are porphyritic in texture and contain large phenocrysts of plagioclase and pyroxene in a glassy groundmass containing abundant microlites (Figure 1a-c; Heap and Kennedy, 2016). In total, 17 blocks of andesite were collected and labelled from R1 to R17 (labels used here are the same as in Heap and Kennedy, 2016). Apart from the presence of rare pore-filling cristobalite in four of the low-porosity samples (indicated in Tables 2 and 3), the blocks from Mt. Ruapehu are not visibly altered (from hand-sample inspection and microstructural observations; see Heap and Kennedy, 2016). The porosity of the samples comprises both pores and microcracks (Figure 1a-c).

The basaltic-andesites from Merapi volcano (Indonesia; Voight et al., 2000; Surono et al., 2012; Kushnir et al., 2016), collected from the summit area of the volcano (from the 1902 lava dome, about 100 m to the northeast of the currently active dome), are characterised by a porphyritic texture comprising phenocrysts of dominantly plagioclase and pyroxene within a crystallised groundmass (plagioclase, K-feldspar, and pyroxene; Figure 1d-e; see Heap et al., 2019a). In total, five blocks of basaltic-andesite were collected and classified in terms of their alteration (based on the wt.% of alteration minerals determined by X-ray powder diffraction; Table 1; Heap et al., 2019a). The alteration phases present, indicative of exposure to acid-sulfate fluids, include natroalunite, alunite, quartz, hematite, cristobalite, gypsum, and unclassified amorphous phases (Figure 1d-e; Table 1; Heap et al., 2019a). The five

blocks from Merapi volcano were labelled M-U ("unaltered"), M-SA1 and M-SA2 ("slightly altered"), and M-HA1 and M-HA2 ("highly altered"). The labels for these materials are the same as in Heap et al. (2019a). The porosity of the samples comprises both pores and microcracks (Figure 1d-e).

Multiple cylindrical samples, 20 mm in diameter, were cored from the blocks collected and their ends were cut and ground flat and parallel to a nominal length of 40 mm. These samples were then dried under vacuum at 40 °C for at least 48 h. The dry bulk sample density was measured for each sample using the dry mass and the bulk sample volume determined using the sample dimensions. The connected porosities of the cylindrical samples were calculated using the skeletal volume measured by a helium pycnometer (Micromeritics AccuPyc II 1340) and the bulk sample volume.

The thermal conductivity, λ (in $W.m^{-1}.K^{-1}$), and thermal diffusivity, D (in $mm^2.s^{-1}$), of each sample was measured using a Hot Disk TPS 500 Thermal Constants Analyser using the transient plane source (TPS) method (outlined in Gustafsson, 1991; Gustavsson et al., 1994; Harlé et al., 2019). The TPS method is a periodic method of thermal property measurement (see the review by Hofmeister, 2019). The standard uncertainty for values of thermal conductivity and thermal diffusivity using the transient hot-strip method has been determined to be 2.6 and 11%, respectively (Hammerschmidt and Sabuga, 2000). Measurement uncertainty using this technique arises from contact losses and ballistic radiative transfer gains (Hofmeister, 2019).

A sensor consisting of two 10 μm-thick nickel foil spirals (radius = 3.189 mm) insulated on both sides by 30 μm-thick kapton (Figure 2, inset) was sandwiched between the cylindrical sample and a piece of polyurethane foam of known thermal properties (Figure 2). The sample and foam piece were held in place using a screw

187 positioned at the top of the sample jig (Figure 2), which ensured good contact
188 between the surface of the sample and the sensor. The temperature adjacent to the
189 sample was measured using a thermocouple and was inputted into the system prior to
190 launching each measurement. During the measurement, an electrical current of known
191 power and duration was passed through the sensor, which also recorded the increase
192 in sample temperature as a function of time. The output power and duration required
193 for a reliable measurement varied from sample to sample and were found using trial-
194 and-error. Four consecutive measurements were performed on each sample and we
195 report herein an average of these four measurements (standard deviations are provided
196 in Tables 2 and 3). Each measurement was performed at least five min apart to ensure
197 that the sample had cooled back to the ambient temperature. The sensor measured the
198 temperature drift of the sample for 40 s prior to each measurement to check whether
199 the sample was in thermal equilibrium. If the sample temperature was not constant
200 during this 40 s period, the data were not considered and the measurement was
201 repeated. "Wet" measurements were performed on samples saturated under vacuum
202 with deionised water, a method that ensures the complete saturation of the connected
203 void space. The wet mass of these samples was first measured in order to calculate the
204 bulk sample density of the water-saturated samples. To perform the wet thermal
205 property measurements, the entire jig (Figure 2) was submersed in a water bath. Wet
206 measurements were performed with the sensor sandwiched between two cylindrical
207 samples cored from the same block (of identical or very similar porosity) of material,
208 rather than using the polyurethane foam described above. The specific heat per unit
209 volume, $\rho_b C_p$ (in J/m^{3}K), provided by the Hot Disk device was divided by the bulk
210 sample density, ρ_b, to provide the bulk sample specific heat capacity, C_p (in kJ.kg^{-1}.K^{-1}).
211 All measurements were conducted in a far-field environment that was at ambient

212 laboratory temperature (ranging from 19 to 27 °C for the dry measurements and 18 to
213 20 °C for the wet measurements) and pressure (~100,000 Pa).
214
215 **3 Results**
216 Bulk sample density, specific heat capacity, and thermal conductivity are
217 plotted as a function of connected porosity in Figure 3 (data available in Tables 2 and
218 3). We first note that bulk sample density decreases linearly as a function of
219 increasing porosity for the dry samples from Mt. Ruapehu (black circles in Figure 3a),
220 suggesting that the volume of isolated porosity is constant over the porosity range or
221 that the volume of isolated porosity in the studied samples is negligible. Although the
222 bulk density of the dry samples from Merapi volcano decreases as a function of
223 increasing porosity (green squares in Figure 3a), the trend is much more scattered
224 than that for the dry Mt. Ruapehu samples.
225 The specific heat capacity of the dry Mt. Ruapehu samples varies between
226 0.591 and 0.856 $kJ.kg^{-1}.K^{-1}$, but does not vary systematically with porosity (black
227 circles in Figure 3b; Table 2). The specific heat capacity of the samples from Merapi
228 volcano also does not vary systematically with porosity (green squares in Figure 3b).
229 The thermal conductivity of the dry Mt. Ruapehu (black circles in Figure 3c)
230 and Merapi volcano (green squares in Figure 3c) samples decreases as a function of
231 increasing porosity. For example, at low porosity (<0.05), the thermal conductivity of
232 the dry samples from Mt. Ruapehu is between ~1.4 and ~1.6 $W.m^{-1}.K^{-1}$, but is as low
233 as ~0.4 $W.m^{-1}.K^{-1}$ when the porosity is ~0.6 (Figure 3c).
234 The thermal diffusivity of the dry Mt. Ruapehu (black circles in Figure 4) and
235 Merapi volcano (green squares in Figure 4) samples decreases as a function of
236 increasing porosity, but the trend is more scattered than that for the thermal

conductivity (Figure 3c). For example, the thermal diffusivity of the dry samples from Mt. Ruapehu decreases from ~0.7-0.8 to ~0.5-0.55 $mm^2.s^{-1}$ as porosity increases from <0.05 to ~0.6 (Figure 4).

When saturated with water, the bulk density (Figure 3a), specific heat capacity (Figure 3b), and thermal conductivity (Figure 3c) of the andesites from Mt. Ruapehu increased, and the thermal diffusivity decreased, relative to the dry state (Figure 4). Our data also show that the influence of water saturation on the thermal properties of the andesites from Mt. Ruapehu depends on the porosity (Figure 5). At low porosity (<0.05), the dry and wet thermal properties are essentially equal, but, at the maximum porosity of ~0.6, the specific heat capacity and thermal conductivity increased by a factor of ~4.5 and ~2.25, respectively (Figures 5a and 5c), and the thermal diffusivity decreased by a factor of ~0.5 (Figure 5c).

For a given porosity, the dry altered basaltic-andesites from Merapi volcano (green squares) have a higher density (Figure 3a), a higher specific heat capacity (Figure 3b), and a lower thermal conductivity (Figure 3c) and thermal diffusivity (Figure 4) than the dry andesites from Mt. Ruapehu. For example, at a porosity of 0.2, the thermal conductivity and thermal diffusivity of the rocks from Merapi volcano are ~0.4 $W.m^{-1}.K^{-1}$ and ~0.2 $mm^2.s^{-1}$ lower than respective values for the andesites from Mt. Ruapehu (Figures 3c and 4).

4 Discussion

A decrease in thermal conductivity, thermal diffusivity, and specific heat capacity as porosity increases for the dry samples (Figures 3 and 4) can be explained by the large difference in these thermal properties between rock-forming minerals and pore-filling air. A decrease in thermal properties as a function of increasing porosity

has been observed previously for dry porous rocks (e.g., Robertson and Peck, 1974; Brigaud and Vasseur, 1989; Clauser and Huenges, 1995; Popov et al., 2003; Pimienta et al., 2014; Esteban et al., 2015; Mielke et al., 2015, 2017; Heap et al., 2019b; Harlé et al., 2019). The change in thermal properties following water saturation (Figure 5) reflects the different thermal properties of pore-filling air and water (e.g., Nagaraju and Roy, 2014; Harlé et al., 2019): the thermal conductivity of air and water are ~0 and ~0.6 $W.m^{-1}.K^{-1}$, respectively. Finally, the reduction in thermal conductivity (Figure 3c) and thermal diffusivity (Figure 4) following hydrothermal alteration, for a given porosity, is interpreted here as the result of differences between the thermal properties of the primary and alteration minerals. Gypsum (one of the alteration minerals; Table 1), for example, has a very low thermal conductivity (Clauser and Huenges, 1995). The influence of hydrothermal alteration on the thermal properties of volcanic rock will also depend on whether the alteration increases or decreases porosity. For example, the alteration of ash tuff from the Tauhara geothermal field decreased porosity, resulting in an increase in thermal conductivity (Mielke et al., 2015).

4.1 Theoretical predictions

The effective thermal conductivity, $\lambda(\phi)$, can be determined using the Maxwell equation:

$$\frac{\lambda(\phi)}{\lambda_0} = \frac{(1-\phi)(1-r)+r\beta\phi}{(1-\phi)(1-r)+\beta\phi}, \quad (1)$$

where ϕ is the total porosity, $r = \lambda_f/\lambda_0$ (where λ_0 and λ_f are the thermal conductivities of the rock groundmass and the fluid within the pore space,

287 respectively), and, for spherical pores, $\beta = 3(1-r)/(2+r)$ (Zimmerman, 1989).
288 The Maxwell model assumes no interaction between the spherical pores. To
289 determine thermal conductivity as a function of porosity for our dry and water-
290 saturated samples, we assume that the thermal conductivity of air and water are 0 and
291 0.6 $W.m^{-1}.K^{-1}$, respectively (e.g., Nagaraju and Roy, 2014; Vosteen and
292 Schellschmidt, 2003). Equation (1) well describes the data for the dry (solid black
293 line; Figure 3c) and wet (dashed blue line; Figure 3c) andesites from Mt. Ruapehu,
294 providing a value for λ_0 of 1.50 $W.m^{-1}.K^{-1}$. We also plot data for variably porous dry
295 basalt from Robertson and Peck (1974) in Figure 3c (grey triangles), which are also
296 well described by Equation (1) (see also Horai, 1991). However, although the low-
297 porosity rocks (porosity <0.1) from Merapi volcano, those characterised by low levels
298 of hydrothermal alteration, follow the trend delineated by a λ_0 of 1.50 $W.m^{-1}.K^{-1}$, the
299 more altered rocks, containing a higher porosity (from ~0.15 to ~0.25), fall
300 consistently below the trend (Figure 3c). This discrepancy can be explained by a
301 change in λ_0 as a result of the change in the mineral assemblage due to hydrothermal
302 alteration. Our data show that the minimum possible value of λ_0 for the altered rocks
303 from Merapi volcano, using Equation (1), is 1.10 $W.m^{-1}.K^{-1}$ (dotted green line; Figure
304 3c).

305 The effective thermal diffusivity $D(\phi)$ can be obtained using (e.g., Connor et
306 al., 1997):

307

308 $$D(\phi) = \frac{\lambda(\phi)}{\rho_s C_p (1-\phi) + \rho_f C_{p,f} \phi}, \quad (2)$$

309

where ρ_s and ρ_f are the matrix and pore fluid densities, respectively, and C_p and $C_{p,f}$ are the matrix and pore fluid specific heat capacity, respectively. Based on Equation (2), the effective specific heat capacity $C_p(\phi)$ can be derived as:

$$C_p(\phi) = \frac{\rho_s C_p(1-\phi) + \rho_f C_{p,f}\phi}{\rho_b}. \quad (3)$$

To model the thermal diffusivity and specific heat capacity data for the andesites from Mt. Ruapehu, we use ρ_s = 2750 kg.m^{-3} and C_p = 0.750 kJ.kg^{-1}.K^{-1} (values selected based on our laboratory measurements for the Mt. Ruapehu samples; Table 2), ρ_f = 1.275 kg.m^{-3} and $C_{p,f}$ = 1.007 kJ.kg^{-1}.K^{-1} for air, and ρ_f = 1000 kg.m^{-3} and $C_{p,f}$ = 4.182 kJ.kg^{-1}.K^{-1} for water. We find that Equation (2) can well describe the dry (solid black line in Figure 4) and water-saturated (dashed blue line in Figure 4) thermal diffusivity data for the Mt. Ruapehu andesites. We also find that Equation (3) well describes the dry (solid black line in Figure 3b) and water-saturated (dashed black line in Figure 3b) specific heat capacity data. We also provide theoretical curves, using Equations (1-3), for the wet/dry ratios for the specific heat capacity, thermal conductivity, and thermal diffusivity data (solid black lines in Figure 5). We find that the theoretical predictions for the wet/dry ratios also well describe our experimental data (Figure 5).

The fact that Equations (1-3) can accurately describe the thermal conductivity, thermal diffusivity, and specific heat capacity of the andesites from Ruapehu, despite their microstructural differences (e.g., differences in pore size, pore shape, microcrack density; Figure 1), highlights that porosity exerts a first order control on the thermal properties of porous andesites.

4.2 Case studies: heat loss from a dyke and conduit

It is important to assess whether the measured changes to thermal conductivity, thermal diffusivity, and specific heat capacity as a function of porosity and alteration (Figures 3 and 4; Tables 2 and 3) are sufficient to influence volcanic/geothermal processes. To do so, we model the migration of the 700 °C isotherm with respect to the boundary of a dyke and a conduit by solving the heat equation in 1D for two different coordinate systems: (1) Cartesian (analogous to dyke geometry) and (2) cylindrical (analogous to conduit geometry) coordinates. We explore a scenario in which the magma in the dyke or conduit is stagnant and loses heat to the host-rock through conduction, leading to wholescale cooling of the system. Fick's second law for heat transfer by conduction is given by (Crank, 1979):

$$\frac{\partial T}{\partial t} = \nabla \cdot (D(\phi)\nabla T), \quad (4)$$

where t is the time since the onset of heat transfer, T is the temperature, and $D(\phi)$ is the effective thermal diffusivity. In 1D, the right-hand side of Equation (4) becomes (Crank, 1979, pages 56 and 69):

$$\begin{cases} \frac{\partial}{\partial x}\left(D(\phi)\frac{\partial T}{\partial x}\right); & \text{cartesian coordinates} - \text{ dyke geometry} \\ \frac{1}{r}\frac{\partial}{\partial r}\left(rD(\phi)\frac{\partial T}{\partial r}\right); & \text{cylindrical coordinates} - \text{conduit geometry} \end{cases}$$

In Cartesian coordinates, x represents for the distance from the dyke centre (assuming an axisymmetric dyke) and, in cylindrical coordinates, r represents for the

radial distance from the conduit centre. In both cases we have the same initial conditions at $t = 0$ that $T = T_m$ for $x \leq L$ and $r \leq R$, and $T = T_r$ for $x > L$ and $r > R$, where T_m and T_r are the initial temperature of the magma and the host-rock, respectively, and L and R are the dyke half-width and conduit radius, respectively. T_m is only applied at the start (i.e. $t = 0$) and the magma cools down by conducting heat to the host-rock. We take a range of T_m from 800 to 1200 °C and $T_r = 50$ °C. We consider a pore-free magma and explore the influence of the porosity of the host-rock on the migration of the isotherm (i.e. the cooling of the system). We scale the effect of porosity by decomposing the bulk specific heat capacity using Equation (3), and by using the Maxwell equation for the bulk thermal conductivity (Equation (1)). The use of these theoretical relationships is supported by their accurate description of our experimental data (Figure 3a and 3c) (the maximum and minimum difference between the data and the value predicted by the model are 0.205 and -0.089 $W.m^{-1}.K^{-1}$ and 0.107 and -0.144 $kJ.kg^{-1}.K^{-1}$ for thermal conductivity and specific heat capacity, respectively). We also use our experimental data to constrain the matrix properties of the host-rock, such that ρ = 2750 $kg.m^{-3}$, λ_0 = 1.50 ± 1 $W.m^{-1}.K^{-1}$, and C_p = 0.750 ± 0.010 $kJ.kg^{-1}.K^{-1}$. As above, we use ρ_f = 1.275 $kg.m^{-3}$ and $C_{p,f}$ = 1.007 $kJ.kg^{-1}.K^{-1}$ for air. Our modelling therefore uses data collected at ambient laboratory pressure and temperature (see our "Data limitations" section below). In our simulations of heat transfer, both dyke and conduit centres are insulated (Neumann boundary condition of 0) such that $\partial T/\partial x = \partial T/\partial r = 0$ for all t. The far-field temperature in the host-rock is kept constant at T_r. We take a typical dyke half-width and conduit radius of $L = R = 25$ m. We explicitly acknowledge that our approach does not account for the advection or convection of heat (in the magma and in the host-rock). It is also assumed that no heat is generated. With these conditions, we solve Equation (4)

numerically using a backward-time, centred-space finite difference scheme. The model setup is presented in Figure 6.

The resulting migration of the 700 °C isotherm as a function of time are shown in Figure 7a (dyke geometry) and Figure 8a (conduit geometry), for air-filled pores, initial magma temperatures, T_m, of 800, 1000, and 1200 °C, and host-rock porosities, ϕ, of 0, 0.3, and 0.6. Figures 7a and 8a show that there is a large influence of initial magma temperature on the migration of the isotherm. For example, after 50 days, and for a porosity of 0.3, the isotherm moves 2.7, 1.1, and 0.2 m from the boundary of the dyke at initial magma temperatures of 800, 1000, and 1200 °C, respectively (Figure 7a). The isotherm moves 2.9, 1.2, and 0.4 m from the boundary of the conduit (i.e. inside the conduit) after 50 days (assuming a porosity of 0.3) at initial magma temperatures of 800, 1000, and 1200 °C, respectively (Figure 8a). Host-rock porosity also influences the migration of the isotherm (Figures 7a and 8a). Following 50 days, for an initial magma temperature of 1200 °C, the isotherm moves from the dyke and conduit boundary by 0.4, 0.2, and 0.1 m and 0.6, 0.4, and 0.2 m for host-rock porosities of 0, 0.3, and 0.6, respectively (Figures 7a and 8a).

We additionally approximate the effect of host-rock hydrothermal alteration on the cooling of a dyke and conduit. To do so, the matrix thermal conductivity, λ_0, was changed from 1.50 ± 1 to 1.10 ± 1 $W.m^{-1}.K^{-1}$, as guided by our experimental data (Figure 3c). All other parameters remained unchanged. Figures 7b and 8b show the results (for a host-rock porosity of 0.1, air-filled pores, and an initial magma temperature of 1000 °C) for the dyke and conduit geometries, respectively. It can be seen that host-rock hydrothermal alteration influences the migration of the isotherm (Figures 7b and 8b). For example, after 50 days, the 700 °C isotherm moves from the

406 dyke and conduit boundary by 1.2 and 1.0 m and 1.3 and 1.1 m for λ_0 = 1.50 (i.e.
407 unaltered) and λ_0 = 1.10 $W.m^{-1}.K^{-1}$ (i.e. altered), respectively (Figures 7b and 8b).
408
409 4.3 Data limitations
410 First, as outlined in our methods section, the standard uncertainty of our
411 thermal conductivity and thermal diffusivity measurements is 2.6 and 11%,
412 respectively (Hammerschmidt and Sabuga, 2000). Data collected using the method
413 used suffers from contact losses and ballistic radiative transfer gains (Hofmeister,
414 2019). Second, our measurements were performed at ambient pressure and
415 temperature. For example, an increase in pressure (i.e. depth) will close microcracks
416 (e.g., Vinciguerra et al., 2005; Nara et al., 2011; Zhu et al., 2016), abundant in these
417 materials (Figure 1). A reduction in porosity, due to the closure of microcracks, will
418 likely increase thermal conductivity, thermal diffusivity, and specific heat capacity
419 (Figures 3 and 4; Equation 1). However, we note that microcracks typically only
420 represent a very small proportion of the porosity within a sample due to their very low
421 aspect ratio (e.g., Kranz, 1983). Therefore, our measurements, performed at room
422 pressure, will likely slightly underestimate the thermal properties of volcanic rock at
423 depth. An increase in temperature has been shown to influence the thermal properties
424 of rocks and rock-forming minerals (e.g., Guéguen and Palciauskas, 1994; Nabelek et
425 al., 2010; Guo et al., 2017; Vosteen and Schellschmidt, 2017; Harlé et al., 2019),
426 including volcanic rocks (e.g., Bates et al., 1970; Horai et al., 1970; Petrunin et al.,
427 1971; Fuji and Osako, 1972; Büttner et al., 1998; Romaine et al., 2012; Hofmeister,
428 2019). Compiled thermal diffusivity data for volcanic materials show that the largest
429 differences in thermal diffusivity occur at temperatures below ~300 °C (Figure 9). For
430 example, Romine et al. (2012) found that the thermal diffusivity of rhyolite decreased

from ~0.65 to ~0.55 $mm^2.s^{-1}$ as temperature was increased from ~20 to ~430 °C, but remained constant from ~430 to ~1300 °C. We also note that the differences as a result of porosity variation (data from this study) are as large as the variation in thermal diffusivity as temperature is increased from ~20 to ~1300 °C (Figure 9). Therefore, although our measurements were performed at room temperature and likely overestimate the thermal diffusivity of volcanic rock at high-temperature, relatively small changes in thermal diffusivity between ~300 and ~1300 °C (Figure 9) provides some support for the assumption of a constant thermal diffusivity in our modelling. It is clear, however, that thermal property measurements at high temperature are now required for a range of variably porous volcanic rocks. An increase in temperature can also generate thermal microcracks that will also serve to decrease thermal conductivity and thermal diffusivity (Kant et al., 2017). However, although rocks such as granites are well known to suffer thermal microcracking when exposed to high-temperature (e.g., Homand-Etienne and Houpert, 1989; David et al., 1999; Chaki et al., 2008; Griffiths et al., 2018), the microstructure of some volcanic rocks is unaffected (e.g., Vinciguerra et al., 2005; Heap et al., 2018; Coats et al., 2018; Eggertsson et al., 2018). Measuring the thermal properties for a range of volcanic rocks at a range of pressures and temperatures offers an exciting avenue for future research.

4.4 Implications

The thermal property data provided herein (Tables 2 and 3) can be used for a wide range of modelling endeavours. We note that, because Equations (1-3) are suitable approximations for the data collected for this study (Figures 3 and 4), the thermal property structure of a volcano or volcanic environment could be estimated

using geophysical methods that provide images of the subsurface in terms of density or porosity, such as muon tomography (Tanaka et al., 2010; Marteau et al., 2012; Lesparre et al., 2012; Rosas-Carbajal et al., 2017). Therefore, if the saturation state of the edifice is known, or can be approximated, Equations (1-3) could be used to estimate the thermal property structure of a volcano that could, in turn, be employed to model heat flow within a volcanic edifice.

Our modelling (Figures 7 and 8) also highlights that hydrothermal alteration slows the cooling of a dyke and conduit. Therefore, progressive hydrothermal alteration of an edifice or lava dome could keep a conduit-dwelling magma or the core of a dome hotter for longer, respectively. Indeed, the maintenance of these elevated temperatures may promote further alteration within the edifice or dome. Hydrothermal alteration of volcanic rocks can result in decreases to rock strength (e.g., Pola et al., 2012; Wyering et al., 2014; Frolova et al., 2014; Heap et al., 2015; Farquharson et al., 2019; Mordensky et al., 2019). Thus, as edifices remain under temperature and fluid conditions amenable to alteration, their structure may become progressively unstable and more prone to mass-wasting events (e.g., López and Williams, 1993; Reid et al., 2001; Finn et al., 2001; Ball et al., 2013, 2015). The volume of edifice material available to such events will be, in part, defined by the extent of alteration, where planes of failure are more likely to be found in areas with extensive alteration. An increase in the spatial distribution and/or intensity of alteration will also hasten permeability reductions as a result of pore- and crack-filling alteration, a process linked to erratic explosive behaviour (Heap et al., 2019a). We further note that recent discrete element modelling has shown that the volume of material in a dome collapse is larger when the ductile core of the dome is smaller, as it controls the depth to which a shear plane can form (Harnett et al., 2018). Therefore,

481 if the hydrothermal alteration of the talus rocks forming the outer shell of a lava dome
482 can inhibit the cooling of the ductile dome core, hydrothermal alteration could limit
483 the volume of material mobilised during the collapse of a lava dome. We consider it
484 important, therefore, to monitor the extent and progression of hydrothermal alteration
485 at active volcanoes using geophysical methods such as electrical tomography (e.g.,
486 Rosas-Carbajal et al., 2016; Byrdina et al., 2017; Soueid Ahmed et al., 2018;
487 Ghorbani et al., 2018), gas monitoring (e.g., de Moor et al., 2019), or methods such as
488 visible and infrared spectroscopy (Crowley et al., 1997; John et al., 2008) and
489 hyperspectral analysis (Kereszturi et al., 2018).
490

491 **5 Conclusions**

492 The thermal properties of volcanic rocks are sought-after parameters for
493 numerous modelling endeavours. Here we present laboratory-measured values of
494 thermal conductivity, thermal diffusivity, and specific heat capacity of variably
495 porous andesites. Our data show that thermal conductivity, thermal diffusivity, and
496 specific heat capacity of dry andesites all decrease as a function of increasing
497 porosity. Relative to the dry state, saturation with water increases the thermal
498 conductivity and specific heat capacity of the andesites, but decreases their thermal
499 diffusivity. Additionally, our data show that hydrothermal alteration, specifically
500 acid-sulphate alteration, increases the specific heat capacity and decreases the thermal
501 conductivity and thermal diffusivity. We find that the measured experimental values
502 agree well with theoretical predictions, suggesting that, despite the microstructural
503 complexity of volcanic rocks, porosity is the principal parameter dictating their
504 thermal properties. To understand whether the measured changes in thermal
505 properties are sufficient to influence natural processes, we provide modelling that

shows how the cooling of a dyke and conduit is slowed by a higher host-rock porosity and by increasing host-rock hydrothermal alteration. The values of thermal conductivity, thermal diffusivity, and specific heat capacity provided herein can help improve modelling designed to inform on volcanic and geothermal processes.

Acknowledgements

This study received funding from LABEX grant ANR-11-LABX-0050_G-EAU-THERMIE-PROFONDE and therefore benefited from state funding managed by the Agence National de la Recherche (ANR) as part of the "Investissements d'avenir" program. V.R.T. and F.M.D. acknowledge funding from the Swedish Research Council (Vetenskapsrådet). Special thanks to Harry Keys and Blake McDavitt (previously at the New Zealand Department of Conservation), Ngati Tuwharetoa, Ngati Rangi, and Ruapehu Alpine Lifts for providing access and permission to sample at Ruapehu. We also thank Nadhirah Seraphine for logistical support and Hanik Humaida at the Balai Penyelidikan dan Pengembangan Teknologi Kebencanaan Geologi (BPPTKG, Yogyakarta) for rewarding discussions on Merapi volcano. We also thank Olivier Lengliné for valuable assistance. The constructive comments of Ingo Sonder and two anonymous reviewers helped improve the clarity of this manuscript.

Author contributions

M.J.H led the project and wrote the manuscript. A.R.L.K. and P.H. measured the dry and wet thermal properties, respectively. J.V. performed the modelling. M.J.H., B.K., V.R.T., and F.M.D. collected the samples used in this study. All of the authors contributed to the interpretation of the data and the writing of the manuscript.

References

Annen, C., Pichavant, M., Bachmann, O., & Burgisser, A. (2008). Conditions for the growth of a long-lived shallow crustal magma chamber below Mount Pelée volcano (Martinique, Lesser Antilles Arc). Journal of Geophysical Research: Solid Earth, 113(B7).

Annen, C. (2017). Factors affecting the thickness of thermal aureoles. *Frontiers in Earth Science*, *5*, 82.

Bagdassarov, N., & Dingwell, D. (1994). Thermal properties of vesicular rhyolite. Journal of Volcanology and Geothermal Research, 60(2), 179-191.

Ball, J. L., Calder, E. S., Hubbard, B. E., & Bernstein, M. L. (2013). An assessment of hydrothermal alteration in the Santiaguito lava dome complex, Guatemala: implications for dome collapse hazards. *Bulletin of Volcanology*, *75*(1), 676.

Ball, J. L., Stauffer, P. H., Calder, E. S., & Valentine, G. A. (2015). The hydrothermal alteration of cooling lava domes. *Bulletin of Volcanology*, *77*(12), 102.

Bates, J. L., McNeilly, C. E., & Rasmussen, J. J. (1970). *Properties of Molten Ceramics. Batelle Memorial Institute, Richland*. Washington BNWL-SA-3529.

Bauer, S. J., & Handin, J. (1983). Thermal expansion and cracking of three confined water-saturated igneous rocks to 800 C. *Rock Mechanics and Rock Engineering*, *16*(3), 181-198.

Bodvarsson, G. S., Pruess, K., Stefansson, V., & Eliasson, E. T. (1984). The Krafla geothermal field, Iceland: 2. The natural state of the system. Water Resources Research, 20(11), 1531-1544.

Brigaud, F., & Vasseur, G. (1989). Mineralogy, porosity and fluid control on thermal conductivity of sedimentary rocks. Geophysical Journal International, 98(3), 525-542.

Bruce, P. M., & Huppert, H. E. (1989). Thermal control of basaltic fissure eruptions. Nature, 342(6250), 665.

Büttner, R., Zimanowski, B., Blumm, J., & Hagemann, L. (1998). Thermal conductivity of a volcanic rock material (olivine-melilitite) in the temperature range between 288 and 1470 K. *Journal of Volcanology and Geothermal Research*, *80*(3-4), 293-302.

Byrdina, S., Friedel, S., Vandemeulebrouck, J., Budi-Santoso, A., Suryanto, W., Rizal, M. H., & Winata, E. (2017). Geophysical image of the hydrothermal system of Merapi volcano. Journal of Volcanology and Geothermal Research, 329, 30-40.

Carrigan, C. R. (1984). Time and temperature dependent convection models of cooling reservoirs: application to volcanic sills. Geophysical Research Letters, 11(8), 693-696.

Carrigan, C. R., Schubert, G., & Eichelberger, J. C. (1992). Thermal and dynamical regimes of single-and two-phase magmatic flow in dikes. Journal of Geophysical Research: Solid Earth, 97(B12), 17377-17392.

Chaki, S., Takarli, M., & Agbodjan, W. P. (2008). Influence of thermal damage on physical properties of a granite rock: porosity, permeability and ultrasonic wave evolutions. *Construction and Building Materials*, *22*(7), 1456-1461.

Chiodini, G., Frondini, F., Cardellini, C., Granieri, D., Marini, L., & Ventura, G. (2001). CO2 degassing and energy release at Solfatara volcano, Campi Flegrei, Italy. Journal of Geophysical Research: Solid Earth, 106(B8), 16213-16221.

579 Clauser, C., & Huenges, E. (1995). Thermal conductivity of rocks and minerals. Rock
580 physics & phase relations: a handbook of physical constants, 3, 105-126.
581 Coats, R., Kendrick, J. E., Wallace, P. A., Miwa, T., Hornby, A. J., Ashworth, J. D.,
582 ... & Lavallée, Y. (2018). Failure criteria for porous dome rocks and lavas: a
583 study of Mt. Unzen, Japan. *Solid Earth*, *9*(6), 1299-1328.
584 Connor, C. B., Lichtner, P. C., Conway, F. M., Hill, B. E., Ovsyannikov, A. A.,
585 Federchenko, I., ... & Taran, Y. A. (1997). Cooling of an igneous dike 20 yr
586 after intrusion. Geology, 25(8), 711-714.
587 Crank, J. (1979). *The Mathematics of Diffusion*. Oxford University Press.
588 Crowley, J. K., & Zimbelman, D. R. (1997). Mapping hydrothermally altered rocks
589 on Mount Rainier, Washington, with airborne visible/infrared imaging
590 spectrometer (AVIRIS) data. *Geology*, *25*(6), 559-562.
591 Currenti, G., Bonaccorso, A., Del Negro, C., Scandura, D., & Boschi, E. (2010).
592 Elasto-plastic modeling of volcano ground deformation. Earth and Planetary
593 Science Letters, 296(3-4), 311-318.
594 David, C., Menéndez, B., & Darot, M. (1999). Influence of stress-induced and
595 thermal cracking on physical properties and microstructure of La Peyratte
596 granite. *International Journal of Rock Mechanics and Mining Sciences*, *36*(4),
597 433-448.
598 de Moor, J. M., Stix, J., Avard, G., Muller, C., Corrales, E., Diaz, J. A., ... & Fischer,
599 T. P. (2019). Insights on Hydrothermal-Magmatic Interactions and Eruptive
600 Processes at Poás Volcano (Costa Rica) From High-Frequency Gas Monitoring
601 and Drone Measurements. *Geophysical Research Letters*, *46*(3), 1293-1302.
602 Del Negro, C., Currenti, G., & Scandura, D. (2009). Temperature-dependent
603 viscoelastic modeling of ground deformation: application to Etna volcano
604 during the 1993–1997 inflation period. Physics of the Earth and Planetary
605 Interiors, 172(3-4), 299-309.
606 De Natale, G., Troise, C., Trigila, R., Dolfi, D., & Chiarabba, C. (2004). Seismicity
607 and 3-D substructure at Somma–Vesuvius volcano: evidence for magma
608 quenching. Earth and Planetary Science Letters, 221(1-4), 181-196.
609 Eggertsson, G. H., Lavallée, Y., Kendrick, J. E., & Markússon, S. H. (2018).
610 Improving fluid flow in geothermal reservoirs by thermal and mechanical
611 stimulation: The case of Krafla volcano, Iceland. *Journal of Volcanology and*
612 *Geothermal Research*.
613 Ehara, S. (1992). Thermal structure beneath Kuju volcano, central Kyushu, Japan.
614 Journal of Volcanology and Geothermal Research, 54(1-2), 107-115.
615 Esteban, L., Pimienta, L., Sarout, J., Delle Piane, C., Haffen, S., Géraud, Y., &
616 Timms, N. E. (2015). Study cases of thermal conductivity prediction from P-
617 wave velocity and porosity. Geothermics, 53, 255-269.
618 Farquharson, J. I., Wild, B., Kushnir, A. R., Heap, M. J., Baud, P., & Kennedy, B.
619 (2019). Acid-Induced Dissolution of Andesite: Evolution of Permeability and
620 Strength. Journal of Geophysical Research: Solid Earth, 124(1), 257-273.
621 Fialko, Y. A., & Rubin, A. M. (1999). Thermal and mechanical aspects of magma
622 emplacement in giant dike swarms. Journal of Geophysical Research: Solid
623 Earth, 104(B10), 23033-23049.
624 Finn, C. A., Sisson, T. W., & Deszcz-Pan, M. (2001). Aerogeophysical measurements
625 of collapse-prone hydrothermally altered zones at Mount Rainier
626 volcano. *Nature*, *409*(6820), 600.
627 Flóvenz, Ó. G., & Saemundsson, K. (1993). Heat flow and geothermal processes in
628 Iceland. Tectonophysics, 225(1-2), 123-138.

Fournier, N., & Chardot, L. (2012). Understanding volcano hydrothermal unrest from geodetic observations: Insights from numerical modeling and application to White Island volcano, New Zealand. Journal of Geophysical Research: Solid Earth, 117(B11).

Frolova, J., Ladygin, V., Rychagov, S., & Zukhubaya, D. (2014). Effects of hydrothermal alterations on physical and mechanical properties of rocks in the Kuril–Kamchatka island arc. Engineering Geology, 183, 80-95.

Fujii, N., & Osako, M. (1973). Thermal diffusivity of lunar rocks under atmospheric and vacuum conditions. *Earth and Planetary Science Letters*, *18*(1), 65-71.

Ghorbani, A., Revil, A., Coperey, A., Ahmed, A. S., Roque, S., Heap, M. J., ... & Viveiros, F. (2018). Complex conductivity of volcanic rocks and the geophysical mapping of alteration in volcanoes. *Journal of Volcanology and Geothermal Research*, *357*, 106-127.

Graham, I. J., Cole, J. W., Briggs, R. M., Gamble, J. A., & Smith, I. E. M. (1995). Petrology and petrogenesis of volcanic rocks from the Taupo Volcanic Zone: a review. *Journal of Volcanology and Geothermal Research*, *68*(1-3), 59-87.

Griffiths, L., Lengliné, O., Heap, M. J., Baud, P., & Schmittbuhl, J. (2018). Thermal cracking in Westerly Granite monitored using direct wave velocity, coda wave interferometry, and acoustic emissions. *Journal of Geophysical Research: Solid Earth*, *123*(3), 2246-2261.

Guo, P. Y., Zhang, N., He, M. C., & Bai, B. H. (2017). Effect of water saturation and temperature in the range of 193 to 373 K on the thermal conductivity of sandstone. *Tectonophysics*, *699*, 121-128.

Gustafsson, S. E. (1991). Transient plane source techniques for thermal conductivity and thermal diffusivity measurements of solid materials. Review of Scientific Instruments, 62(3), 797-804.

Gustavsson, M., Karawacki, E., & Gustafsson, S. E. (1994). Thermal conductivity, thermal diffusivity, and specific heat of thin samples from transient measurements with hot disk sensors. Review of Scientific Instruments, 65(12), 3856-3859.

Hackett, W. R., & Houghton, B. F. (1989). A facies model for a Quaternary andesitic composite volcano: Ruapehu, New Zealand. Bulletin of volcanology, 51(1), 51-68.

Hammerschmidt, U., & Sabuga, W. (2000). Transient hot strip (THS) method: uncertainty assessment. *International Journal of Thermophysics*, *21*(1), 217-248.

Harlé, P., Kushnir, A. R., Aichholzer, C., Heap, M. J., Hehn, R., Maurer, V., ... & Duringer, P. (2019). Heat flow density estimates in the Upper Rhine Graben using laboratory measurements of thermal conductivity on sedimentary rocks. *Geothermal Energy*, *7*(1), 1-36.

Harnett, C. E., Thomas, M. E., Purvance, M. D., & Neuberg, J. (2018). Using a discrete element approach to model lava dome emplacement and collapse. *Journal of Volcanology and Geothermal Research*, *359*, 68-77.

Harris, A. J., & Stevenson, D. S. (1997). Thermal observations of degassing open conduits and fumaroles at Stromboli and Vulcano using remotely sensed data. Journal of Volcanology and Geothermal Research, 76(3-4), 175-198.

Harris, A. J., Blake, S., Rothery, D. A., & Stevens, N. F. (1997). A chronology of the 1991 to 1993 Mount Etna eruption using advanced very high resolution radiometer data: Implications for real-time thermal volcano monitoring. Journal of Geophysical Research: Solid Earth, 102(B4), 7985-8003.

679 Heap, M. J., Kolzenburg, S., Russell, J. K., Campbell, M. E., Welles, J., Farquharson,
680 J. I., & Ryan, A. (2014). Conditions and timescales for welding block-and-ash
681 flow deposits. *Journal of Volcanology and Geothermal Research*, *289*, 202-209.
682 Heap, M. J., Kennedy, B. M., Pernin, N., Jacquemard, L., Baud, P., Farquharson, J. I.,
683 ... & Mayer, K. (2015). Mechanical behaviour and failure modes in the
684 Whakaari (White Island volcano) hydrothermal system, New Zealand. Journal
685 of Volcanology and Geothermal Research, 295, 26-42.
686 Heap, M. J., & Kennedy, B. M. (2016). Exploring the scale-dependent permeability of
687 fractured andesite. Earth and Planetary Science Letters, 447, 139-150.
688 Heap, M. J., Violay, M., Wadsworth, F. B., & Vasseur, J. (2017a). From rock to
689 magma and back again: The evolution of temperature and deformation
690 mechanism in conduit margin zones. Earth and Planetary Science Letters, 463,
691 92-100.
692 Heap, M. J., Kennedy, B. M., Farquharson, J. I., Ashworth, J., Mayer, K., Letham-
693 Brake, M., ... & Siratovich, P. (2017b). A multidisciplinary approach to quantify
694 the permeability of the Whakaari/White Island volcanic hydrothermal system
695 (Taupo Volcanic Zone, New Zealand). Journal of Volcanology and Geothermal
696 Research, 332, 88-108.
697 Heap, M. J., Coats, R., Chen, C. F., Varley, N., Lavallée, Y., Kendrick, J., ... &
698 Reuschlé, T. (2018). Thermal resilience of microcracked andesitic dome rocks.
699 Journal of Volcanology and Geothermal Research, 367, 20-30.
700 Heap, M. J., Troll, V. R., Kushnir, A. R. L., Gilg, H. A., Collinson, A. S. D., Deegan,
701 F. M., Darmawan, H., Seraphine, N., Neuberg, J., & Walter, T. R. (2019a).
702 Hydrothermal alteration of andesitic lava domes can lead to explosive volcanic
703 behaviour. Nature Communications, doi: 10.1038/s41467-019-13102-8.
704 Heap, M. J., Kushnir, A. R., Gilg, H. A., Violay, M. E., Harlé, P., & Baud, P. (2019b).
705 Petrophysical properties of the Muschelkalk from the Soultz-sous-Forêts
706 geothermal site (France), an important lithostratigraphic unit for geothermal
707 exploitation in the Upper Rhine Graben. *Geothermal Energy*, *7*(1), 27.
708 Hofmeister, A. (2019). Measurements, Mechanisms, and Models of Heat Transport,
709 Elsevier.
710 Homand-Etienne, F., & Houpert, R. (1989). Thermally induced microcracking in
711 granites: characterization and analysis. International Journal of Rock Mechanics
712 and Mining Sciences, 26, No. 2, 125-134.
713 Horai, K. I., Simmons, G., Kanamori, H., & Wones, D. (1970). Thermal diffusivity
714 and conductivity of lunar material. *Science*, *167*(3918), 730-731.
715 Horai, K. I. (1991). Thermal conductivity of Hawaiian basalt: A new interpretation of
716 Robertson and Peck's data. *Journal of Geophysical Research: Solid*
717 *Earth*, *96*(B3), 4125-4132.
718 Hurwitz, S., Ingebritsen, S. E., & Sorey, M. L. (2002). Episodic thermal perturbations
719 associated with groundwater flow: An example from Kilauea Volcano, Hawaii.
720 Journal of Geophysical Research: Solid Earth, 107(B11).
721 Hurwitz, S., Kipp, K. L., Ingebritsen, S. E., & Reid, M. E. (2003). Groundwater flow,
722 heat transport, and water table position within volcanic edifices: Implications
723 for volcanic processes in the Cascade Range. Journal of Geophysical Research:
724 Solid Earth, 108(B12).
725 Hutchison, W., Varley, N., Pyle, D. M., Mather, T. A., & Stevenson, J. A. (2013).
726 Airborne thermal remote sensing of the Volcán de Colima (Mexico) lava dome
727 from 2007 to 2010. Geological Society, London, Special Publications, 380(1),
728 203-228.

729 Irvine, T. N. (1970). Heat transfer during solidification of layered intrusions. I. Sheets
730 and sills. *Canadian Journal of Earth Sciences*, *7*(4), 1031-1061.
731 John, D. A., Sisson, T. W., Breit, G. N., Rye, R. O., & Vallance, J. W. (2008).
732 Characteristics, extent and origin of hydrothermal alteration at Mount Rainier
733 Volcano, Cascades Arc, USA: Implications for debris-flow hazards and mineral
734 deposits. *Journal of Volcanology and Geothermal Research*, *175*(3), 289-314.
735 Kereszturi, G., Schaefer, L. N., Schleiffarth, W. K., Procter, J., Pullanagari, R. R.,
736 Mead, S., & Kennedy, B. (2018). Integrating airborne hyperspectral imagery
737 and LiDAR for volcano mapping and monitoring through image
738 classification. *International Journal of Applied Earth Observation and*
739 *Geoinformation*, *73*, 323-339.
740 Kühn, M., & Stöfen, H. (2005). A reactive flow model of the geothermal reservoir
741 Waiwera, New Zealand. Hydrogeology Journal, 13(4), 606-626.
742 Kushnir, A. R., Martel, C., Bourdier, J. L., Heap, M. J., Reuschlé, T., Erdmann, S., ...
743 & Cholik, N. (2016). Probing permeability and microstructure: unravelling the
744 role of a low-permeability dome on the explosivity of Merapi
745 (Indonesia). *Journal of Volcanology and Geothermal Research*, *316*, 56-71.
746 Kranz, R. L. (1983). Microcracks in rocks: a review. Tectonophysics, 100(1-3), 449-
747 480.
748 Lesparre, N., Gibert, D., Marteau, J., Komorowski, J. C., Nicollin, F., & Coutant, O.
749 (2012). Density muon radiography of La Soufriere of Guadeloupe volcano:
750 comparison with geological, electrical resistivity and gravity data. *Geophysical*
751 *Journal International*, *190*(2), 1008-1019.
752 Lamur, A., Lavallée, Y., Iddon, F. E., Hornby, A. J., Kendrick, J. E., von Aulock, F.
753 W., & Wadsworth, F. B. (2018). Disclosing the temperature of columnar
754 jointing in lavas. *Nature Communications*, *9*(1), 1432.
755 López, D. L., & Williams, S. N. (1993). Catastrophic volcanic collapse: relation to
756 hydrothermal processes. *Science*, *260*(5115), 1794-1796.
757 Marteau, J., Gibert, D., Lesparre, N., Nicollin, F., Noli, P., & Giacoppo, F. (2012).
758 Muons tomography applied to geosciences and volcanology. *Nuclear*
759 *Instruments and Methods in Physics Research Section A: Accelerators,*
760 *Spectrometers, Detectors and Associated Equipment*, *695*, 23-28.
761 Mattsson, T., Burchardt, S., Almqvist, B. S., & Ronchin, E. (2018). Syn-
762 Emplacement Fracturing in the Sandfell Laccolith, Eastern Iceland—
763 Implications for Rhyolite Intrusion Growth and Volcanic Hazards. *Frontiers in*
764 *Earth Science*, *6*, 5.
765 Mercer, J. W., & Faust, C. R. (1979). Geothermal reservoir simulation: 3. Application
766 of liquid-and vapor-dominated hydrothermal modeling techniques to Wairakei,
767 New Zealand. Water Resources Research, 15(3), 653-671.
768 Mielke, P., Nehler, M., Bignall, G., & Sass, I. (2015). Thermo-physical rock
769 properties and the impact of advancing hydrothermal alteration—A case study
770 from the Tauhara geothermal field, New Zealand. *Journal of Volcanology and*
771 *Geothermal Research*, *301*, 14-28.
772 Mielke, P., Weinert, S., Bignall, G., & Sass, I. (2016). Thermo-physical rock
773 properties of greywacke basement rock and intrusive lavas from the Taupo
774 Volcanic Zone, New Zealand. *Journal of Volcanology and Geothermal*
775 *Research*, *324*, 179-189.
776 Mielke, P., Bär, K., & Sass, I. (2017). Determining the relationship of thermal
777 conductivity and compressional wave velocity of common rock types as a basis
778 for reservoir characterization. *Journal of Applied Geophysics*, *140*, 135-144.

779 Mordensky, S. P., Heap, M. J., Kennedy, B. M., Gilg, H. A., Villeneuve, M. C.,
780 Farquharson, J. I., & Gravley, D. M. (2019). Influence of alteration on the
781 mechanical behaviour and failure mode of andesite: implications for shallow
782 seismicity and volcano monitoring. *Bulletin of Volcanology*, *81*(8), 44.
783 Nabelek, P. I., Whittington, A. G., & Hofmeister, A. M. (2010). Strain heating as a
784 mechanism for partial melting and ultrahigh temperature metamorphism in
785 convergent orogens: Implications of temperature-dependent thermal diffusivity
786 and rheology. *Journal of Geophysical Research: Solid Earth*, *115*(B12).
787 Nabelek, P. I., Hofmeister, A. M., & Whittington, A. G. (2012). The influence of
788 temperature-dependent thermal diffusivity on the conductive cooling rates of
789 plutons and temperature-time paths in contact aureoles. *Earth and Planetary*
790 *Science Letters*, *317*, 157-164.
791 Nagaraju, P., & Roy, S. (2014). Effect of water saturation on rock thermal
792 conductivity measurements. Tectonophysics, 626, 137-143.
793 Nara, Y., Meredith, P. G., Yoneda, T., & Kaneko, K. (2011). Influence of macro-
794 fractures and micro-fractures on permeability and elastic wave velocities in
795 basalt at elevated pressure. *Tectonophysics*, *503*(1-2), 52-59.
796 Norton, D., & Knight, J. (1977). Transport phenomena in hydrothermal systems:
797 cooling plutons. *Am. J. Sci., 277*, DOI: 10.2475/ajs.277.8.937.
798 Oppenheimer, C., Francis, P. W., Rothery, D. A., Carlton, R. W., & Glaze, L. S.
799 (1993). Infrared image analysis of volcanic thermal features: Lascar Volcano,
800 Chile, 1984–1992. Journal of Geophysical Research: Solid Earth, 98(B3), 4269-
801 4286.
802 Petrunin, G.I., Yurehak, R.I., & Tkach, G.F. (1971). Thermal diffusivity of Basalts at
803 Temperatures from 300 to 1220 K. Earth Phys., 2, 65-68.
804 Pimienta, L., Sarout, J., Esteban, L., & Piane, C. D. (2014). Prediction of rocks
805 thermal conductivity from elastic wave velocities, mineralogy and
806 microstructure. Geophysical Journal International, 197(2), 860-874.
807 Pola, A., Crosta, G., Fusi, N., Barberini, V., and Norini, G., 2012, Influence of
808 alteration on physical properties of volcanic rocks: Tectonophysics, v. 566, p.
809 67-86, doi: 10.1016/j.tecto.2012.07.017.
810 Popov, Y., Tertychnyi, V., Romushkevich, R., Korobkov, D., & Pohl, J. (2003).
811 Interrelations between thermal conductivity and other physical properties of
812 rocks: experimental data. In Thermo-Hydro-Mechanical Coupling in Fractured
813 Rock (pp. 1137-1161). Birkhäuser, Basel.
814 Reid, M. E., Sisson, T. W., & Brien, D. L. (2001). Volcano collapse promoted by
815 hydrothermal alteration and edifice shape, Mount Rainier,
816 Washington. *Geology*, *29*(9), 779-782.
817 Robertson, E. C., & Peck, D. L. (1974). Thermal conductivity of vesicular basalt from
818 Hawaii. Journal of Geophysical Research, 79(32), 4875-4888.
819 Romine, W. L., Whittington, A. G., Nabelek, P. I., & Hofmeister, A. M. (2012).
820 Thermal diffusivity of rhyolitic glasses and melts: effects of temperature,
821 crystals and dissolved water. *Bulletin of volcanology*, *74*(10), 2273-2287.
822 Rosas-Carbajal, M., Komorowski, J. C., Nicollin, F., & Gibert, D. (2016). Volcano
823 electrical tomography unveils edifice collapse hazard linked to hydrothermal
824 system structure and dynamics. Scientific Reports, 6, 29899.
825 Rosas-Carbajal, M., Jourde, K., Marteau, J., Deroussi, S., Komorowski, J. C., &
826 Gibert, D. (2017). Three-dimensional density structure of La Soufrière de
827 Guadeloupe lava dome from simultaneous muon radiographies and gravity
828 data. *Geophysical Research Letters*, *44*(13), 6743-6751.

Sammel, E. A., Ingebritsen, S. E., & Mariner, R. H. (1988). The hydrothermal system at Newberry volcano, Oregon. Journal of Geophysical Research: Solid Earth, 93(B9), 10149-10162.

Schauroth, J., Wadsworth, F. B., Kennedy, B., von Aulock, F. W., Lavallée, Y., Damby, D. E., ... & Dingwell, D. B. (2016). Conduit margin heating and deformation during the AD 1886 basaltic Plinian eruption at Tarawera volcano, New Zealand. Bulletin of Volcanology, 78(2), 12.

Siratovich, P. A., von Aulock, F. W., Lavallée, Y., Cole, J. W., Kennedy, B. M., & Villeneuve, M. C. (2015). Thermoelastic properties of the Rotokawa Andesite: a geothermal reservoir constraint. *Journal of Volcanology and Geothermal Research*, *301*, 1-13.

Soueid Ahmed, A., Revil, A., Byrdina, S., Coperey, A., Gailler, L., Grobbe, N., ... & Hogg, C. (2018). 3D electrical conductivity tomography of volcanoes. *Journal of Volcanology and Geothermal Research*, *356*, 243-263.

Surono, Jousset, P., Pallister, J., Boichu, M., Buongiorno, M. F., Budisantoso, A., Costa, F., ... & Humaida, H. (2012). The 2010 explosive eruption of Java's Merapi volcano—a '100-year'event. Journal of Volcanology and Geothermal Research, 241, 121-135.

Tanaka, H. K., Taira, H., Uchida, T., Tanaka, M., Takeo, M., Ohminato, T., ... & Tsuiji, H. (2010). Three-dimensional computational axial tomography scan of a volcano with cosmic ray muon radiography. *Journal of Geophysical Research: Solid Earth*, *115*(B12).

Tsang S, Lindsay, J., Coco., G, Wysocki R. Lerner G., Rader E., Turner G., & Kennedy B. (2019). The heating of substrates beneath basaltic lava flows, *Bulletin of Volcanology*, doi: 10.1007/s00445-019-1320-y

Vélez, M. I., Blessent, D., Córdoba, S., López-Sánchez, J., Raymond, J., & Parra-Palacio, E. (2018). Geothermal potential assessment of the Nevado del Ruiz volcano based on rock thermal conductivity measurements and numerical modeling of heat transfer. *Journal of South American Earth Sciences*, *81*, 153-164.

Vinciguerra, S., Trovato, C., Meredith, P. G., & Benson, P. M. (2005). Relating seismic velocities, thermal cracking and permeability in Mt. Etna and Iceland basalts. *International Journal of Rock Mechanics and Mining Sciences*, *42*(7-8), 900-910.

Violette, S., Ledoux, E., Goblet, P., & Carbonnel, J. P. (1997). Hydrologic and thermal modeling of an active volcano: the Piton de la Fournaise, Reunion. Journal of Hydrology, 191(1-4), 37-63.

Voight, B., Constantine, E. K., Siswowidjoyo, S., & Torley, R. (2000). Historical eruptions of Merapi volcano, central Java, Indonesia, 1768–1998. *Journal of Volcanology and Geothermal Research*, *100*(1-4), 69-138.

Vosteen, H. D., & Schellschmidt, R. (2003). Influence of temperature on thermal conductivity, thermal capacity and thermal diffusivity for different types of rock. *Physics and Chemistry of the Earth, Parts A/B/C*, *28*(9-11), 499-509.

Wadsworth, F. B., Vasseur, J., von Aulock, F. W., Hess, K. U., Scheu, B., Lavallée, Y., & Dingwell, D. B. (2014). Nonisothermal viscous sintering of volcanic ash. Journal of Geophysical Research: Solid Earth, 119(12), 8792-8804.

Wadsworth, F. B., Vasseur, J., Llewellin, E. W., Genareau, K., Cimarelli, C., & Dingwell, D. B. (2017). Size limits for rounding of volcanic ash particles heated by lightning. Journal of Geophysical Research: Solid Earth, 122(3), 1977-1989.

Whittington, A. G., Hofmeister, A. M., & Nabelek, P. I. (2009). Temperature-dependent thermal diffusivity of the Earth's crust and implications for magmatism. *Nature*, *458*(7236), 319.

Wilson, C. J. N., Houghton, B. F., McWilliams, M. O., Lanphere, M. A., Weaver, S. D., & Briggs, R. M. (1995). Volcanic and structural evolution of Taupo Volcanic Zone, New Zealand: a review. *Journal of Volcanology and Geothermal Research*, *68*(1-3), 1-28.

Wooster, M. J., Wright, R., Blake, S., & Rothery, D. A. (1997). Cooling mechanisms and an approximate thermal budget for the 1991–1993 Mount Etna lava flow. Geophysical Research Letters, 24(24), 3277-3280.

Wright, R., Flynn, L. P., Garbeil, H., Harris, A. J., & Pilger, E. (2004). MODVOLC: near-real-time thermal monitoring of global volcanism. Journal of Volcanology and Geothermal Research, 135(1-2), 29-49.

Wyering, L. D., Villeneuve, M. C., Wallis, I. C., Siratovich, P. A., Kennedy, B. M., Gravley, D. M., and Cant, J. L., 2014, Mechanical and physical properties of hydrothermally altered rocks, Taupo Volcanic Zone, New Zealand: Journal of Volcanology and Geothermal Research, v. 288, p. 76-93, doi: 10.1016/j.jvolgeores.2014.10.008.

Zhu, W., Baud, P., Vinciguerra, S., & Wong, T. F. (2016). Micromechanics of brittle faulting and cataclastic flow in Mount Etna basalt. *Journal of Geophysical Research: Solid Earth*, *121*(6), 4268-4289.

Zimmerman, R. W. (1989). Thermal conductivity of fluid-saturated rocks. *Journal of Petroleum Science and Engineering*, *3*(3), 219-227.

Figure captions

Figure 1. Backscattered scanning electron microscope images of select samples from Ruapehu (panels a to c; images from Heap and Kennedy (2016)) and Merapi (panels d to e; images from Heap et al. (2019a)). Important microstructural features are labelled on the images.

Figure 2. Photograph of the experimental setup. The inset shows the detail of the sensor, consisting of two 10 μm-thick nickel foil spirals (radius = 3.189 mm) insulated on both sides by 30 μm-thick kapton.

Figure 3. (a) Bulk sample density, (b) specific heat capacity, and (c) thermal conductivity as a function of connected porosity for the andesites from Mt. Ruapehu and the altered basaltic-andesites from Merapi volcano (see Tables 2 and 3). Solid, dashed, and dotted lines correspond to theoretical curves (see text for details). Blue circles – Mt. Ruapehu (wet); black circles – Mt. Ruapehu (dry); green squares – Merapi volcano (dry); grey triangles – Hawaiian basalt (data from Robertson and Peck, 1974). The standard uncertainty for values of thermal conductivity and thermal diffusivity using the transient hot-strip method has been determined to be 2.6 and 11%, respectively (Hammerschmidt and Sabuga, 2000).

Figure 4. Thermal diffusivity as a function of connected porosity for the andesites from Mt. Ruapehu and the altered basaltic-andesites from Merapi volcano (see Tables 2 and 3). Solid and dashed lines correspond to theoretical curves (see text for details). Blue circles – Mt. Ruapehu (wet); black circles – Mt. Ruapehu (dry); green squares –

927 Merapi volcano (dry). The standard uncertainty for values of thermal diffusivity using
928 the transient hot-strip method has been determined to be 11% (Hammerschmidt and
929 Sabuga, 2000).
930
931 **Figure 5**. The ratio of wet-to-dry (a) thermal conductivity, (b) thermal diffusivity, and
932 (c) specific heat capacity as a function of connected porosity for the samples from Mt.
933 Ruapehu. Solid lines correspond to theoretical curves (see text for details).
934
935 **Figure 6**. Model set up and example results using the thermal properties for the host-
936 rock (or edifice) constrained herein. We present two suites of simplified conduction
937 model, for heat transfer from a dyke (a-c) or from a cylindrical conduit (d-f). Panels
938 (a) and (d) show the general coordinate system (we do not introduce the coordinate
939 directions y, z, or θ in the text because these are implicit in the derivation for each
940 geometry). In panels (b-c) and (e-f), the vertical dashed grey line represents the dyke
941 margin (b-c; $x = L$) or the conduit margin (e-f; $r = R$). In panels (b) and (e) we show
942 the distribution of the porosity across the domain, which is imposed throughout the
943 simulations, where the magma is always at zero porosity, and the country rock has a
944 porosity of 0, 0.3, or 0.6 (each solution type is delineated by line style). In panels (c)
945 and (f) we show an example suite of solutions for the evolution of temperature across
946 the domain for each geometry, and also mark the initial magma temperature T_m
947 (colour delineates the three magma temperatures investigated), and the country rock
948 temperature T_r = 50 °C. The thermal property determinations at low temperature are
949 most applicable to the evolution of temperature in the host-rock far field, relevant to
950 the geothermal system, but we note that these simulations show that the thermal

951 evolution in this host-rock domain depends on the thermal pathway taken by the
952 magma, as well as the geometry of the system.
953
954 **Figure 7**. (a) The migration of the 700 °C isotherm within a dyke (dyke half-width =
955 25 m) as a function of time for an unaltered host-rock with air-filled pores. Modelled
956 curves are provided for different initial magma temperatures (800, 1000, and 1200
957 °C) and different host-rock porosities (0, 0.3, and 0.6). (b) The migration of the 700
958 °C isotherm within a dyke as a function of time for host-rocks with different thermal
959 conductivities chosen to represent unaltered host-rock (λ_0 = 1.50 $W.m^{-1}.K^{-1}$) and
960 hydrothermally altered host-rock (λ_0 = 1.10 $W.m^{-1}.K^{-1}$). Both curves are for an initial
961 magma temperature of 1000 °C and a host-rock porosity of 0.1.
962
963 **Figure 8**. (a) The migration of the 700 °C isotherm within a conduit (conduit radius =
964 25 m) as a function of time for a host-rock with air-filled pores. Modelled curves are
965 provided for different initial magma temperatures (800, 1000, and 1200 °C) and
966 different host-rock porosities (0, 0.3, and 0.6). (b) The migration of the 700 °C
967 isotherm within a conduit as a function of time for host-rocks with different thermal
968 conductivities chosen to represent unaltered host-rock (λ_0 = 1.50 $W.m^{-1}.K^{-1}$) and
969 hydrothermally altered host-rock (λ_0 = 1.10 $W.m^{-1}.K^{-1}$). Both curves are for an initial
970 magma temperature of 1000 °C and a host-rock porosity of 0.1.
971
972 **Figure 9**. Thermal diffusivity for volcanic materials as a function of temperature.
973 Data from: this study, Romine et al. (2012), Büttner et al. (1998), Fuji and Osako
974 (1972), Bates et al. (1970), and Petrunin et al. (1971).

975 **Table 1**. X-ray powder diffraction (XRPD) analysis showing quantitative bulk
976 mineralogical composition for the five blocks from Merapi volcano (in wt.%). The
977 five blocks from Merapi volcano are labelled M-U ("unaltered"), M-SA1 and M-SA2
978 ("slightly altered"), and M-HA1 and M-AH2 ("highly altered") (as in Heap et al.,
979 2019a). An asterisk denotes an alteration phase. Data from Heap et al. (2019a).
980

Mineral	**M-U**	**M-SA1**	**M-SA2**	**M-HA1**	**M-HA2**
Plagioclase	54 ± 3	47 ± 3	38 ± 3	38 ± 3	19 ± 3
K-Feldspar	19 ± 3	9 ± 3	13 ± 3	6 ± 3	10 ± 3
Clinopyroxene ± orthopyroxene	16 ± 2	13 ± 2	14 ± 2	11 ± 2	8 ± 2
Magnetite	3 ± 0.5	2 ± 0.5	2.5 ± 0.5	<1 ± 0.5	<1 ± 0.5
Gypsum*	-	0.5 ± 0.5	4 ± 0.5	5 ± 0.5	6 ± 0.5
K-Na-Alunite*	-	1 ± 0.5	8.5 ± 2	11 ± 2	24 ± 2
Quartz*	1 ± 0.5	1.5 ± 0.5	0.5 ± 0.5	1 ± 0.5	0.5 ± 0.5
Hematite*	0.5 ± 0.5	2 ± 0.5	0.5 ± 0.5	3 ± 0.5	1 ± 0.5
Cristobalite*	6 ± 0.5	-	-	-	2.5 ± 0.5
Amorphous phases*	-	24 ± 4	19 ± 4	25 ± 4	28 ± 4

981

Table 2. Connected porosity, bulk sample density, thermal conductivity, thermal diffusivity, and specific heat capacity of the dry volcanic rocks measured for this study. Asterisk indicates that the sample contains cristobalite (see Heap and Kennedy, 2016; Heap et al., 2019a). The five blocks from Merapi volcano are labelled M-U ("unaltered"), M-SA1 and M-SA2 ("slightly altered"), and M-HA1 and M-AH2 ("highly altered") (as in Heap et al., 2019a). Quoted values of thermal conductivity and thermal diffusivity are the average of four measurements. The specific heat capacity was calculated by dividing the specific heat per unit volume, given by the Hot Disk device (using the average of the four measurements), by the bulk sample density. The standard deviations provided relate to measurement precision (calculated using the four measurements). The standard uncertainty for values of thermal conductivity and thermal diffusivity using the transient hot-strip method has been determined to be 2.6 and 11%, respectively (Hammerschmidt and Sabuga, 2000).

Volcano	Sample number	Bulk sample density, ρ_b (kg.m^{-3})	Connected porosity	Thermal conductivity, λ (W.m^{-1}.K^{-1})	Thermal diffusivity, D (mm^2.s^{-1})	Specific heat capacity, C_p (kJ.kg^{-1}.K^{-1})
Ruapehu	R1-1*	2760	0.021	1.54 ± 0.018	0.70 ± 0.020	0.80 ± 0.032
Ruapehu	R1-2*	2710	0.040	1.62 ± 0.016	0.77 ± 0.018	0.78 ± 0.010
Ruapehu	R2-1*	2714	0.024	1.47 ± 0.064	0.77 ± 0.074	0.72 ± 0.100
Ruapehu	R2-2*	2686	0.036	1.46 ± 0.051	0.75 ± 0.009	0.73 ± 0.016
Ruapehu	R3-1*	2706	0.042	1.53 ± 0.007	0.76 ± 0.035	0.74 ± 0.037
Ruapehu	R3-2*	2692	0.047	1.51 ± 0.050	0.72 ± 0.054	0.79 ± 0.085
Ruapehu	R4-1*	2669	0.038	1.45 ± 0.030	0.70 ± 0.033	0.77 ± 0.053
Ruapehu	R4-2*	2681	0.036	1.51 ± 0.005	0.72 ± 0.007	0.78 ± 0.005
Ruapehu	R5-1	2709	0.024	1.48 ± 0.016	0.71 ± 0.018	0.77 ± 0.028

Ruapehu	R5-2	2704	0.027	1.46 ± 0.031	0.68 ± 0.012	0.79 ± 0.003
Ruapehu	R6-1	2635	0.048	1.39 ± 0.011	0.83 ± 0.056	0.64 ± 0.039
Ruapehu	R6-2	2663	0.042	1.41 ± 0.002	0.67 ± 0.004	0.80 ± 0.004
Ruapehu	R7-1	2260	0.184	1.06 ± 0.010	0.65 ± 0.038	0.73 ± 0.049
Ruapehu	R7-2	2227	0.205	1.00 ± 0.047	0.58 ± 0.055	0.79 ± 0.112
Ruapehu	R8-1	2500	0.098	1.26 ± 0.013	0.70 ± 0.037	0.72 ± 0.045
Ruapehu	R8-2	2455	0.118	1.22 ± 0.058	0.65 ± 0.054	0.77 ± 0.100
Ruapehu	R9-1	2361	0.153	1.17 ± 0.048	0.66 ± 0.081	0.76 ± 0.057
Ruapehu	R9-2	2389	0.140	1.23 ± 0.051	0.71 ± 0.058	0.74 ± 0.080
Ruapehu	R10-1	2372	0.149	1.14 ± 0.043	0.65 ± 0.016	0.73 ± 0.046
Ruapehu	R10-2	2322	0.167	1.08 ± 0.092	0.72 ± 0.094	0.65 ± 0.030
Ruapehu	R11-1	2417	0.129	1.21 ± 0.045	0.59 ± 0.005	0.86 ± 0.039
Ruapehu	R11-2	2361	0.151	1.13 ± 0.052	0.60 ± 0.063	0.80 ± 0.048
Ruapehu	R12-1	2209	0.204	1.01 ± 0.046	0.61 ± 0.029	0.75 ± 0.002
Ruapehu	R12-2	2286	0.182	1.09 ± 0.018	0.62 ± 0.051	0.78 ± 0.051
Ruapehu	R13-1	1924	0.308	0.81 ± 0.004	0.64 ± 0.029	0.66 ± 0.033
Ruapehu	R14-1	1886	0.320	0.84 ± 0.003	0.75 ± 0.108	0.61 ± 0.104
Ruapehu	R14-2	1834	0.345	0.81 ± 0.041	0.52 ± 0.050	0.85 ± 0.046
Ruapehu	R15-1	1817	0.348	0.81 ± 0.060	0.59 ± 0.019	0.76 ± 0.053
Ruapehu	R15-2	1866	0.333	0.79 ± 0.052	0.53 ± 0.065	0.81 ± 0.072
Ruapehu	R16-1	1725	0.382	0.73 ± 0.044	0.63 ± 0.092	0.68 ± 0.138
Ruapehu	R17-1	1068	0.602	0.43 ± 0.026	0.51 ± 0.044	0.79 ± 0.020
Ruapehu	R17-2	999	0.628	0.38 ± 0.027	0.55 ± 0.082	0.71 ± 0.155
Merapi	M-U* 5B-4	2578	0.080	1.43 ± 0.022	0.70 ± 0.038	0.79 ± 0.031
Merapi	M-U* 5B-5	2564	0.084	1.37 ± 0.033	0.73 ± 0.031	0.74 ± 0.023
Merapi	M-U*	2586	0.077	1.48	0.73	0.79

	5B-8			± 0.025	± 0.041	± 0.037
Merapi	M-SA-2 2B-4	2490	0.079	1.20 ± 0.015	0.57 ± 0.022	0.86 ± 0.041
Merapi	M-SA-2 2B-6	2493	0.080	1.23 ± 0.052	0.57 ± 0.027	0.87 ± 0.019
Merapi	M-SA-2 2B-8	2494	0.083	1.28 ± 0.015	0.53 ± 0.021	0.98 ± 0.030
Merapi	M-HA-1 4B-4	2293	0.154	1.07 ± 0.068	0.51 ± 0.030	0.91 ± 0.041
Merapi	M-HA-1 4B-5	2207	0.182	0.90 ± 0.059	0.51 ± 0.028	0.81 ± 0.014
Merapi	M-HA-1 4B-6	2251	0.144	1.07 ± 0.049	0.53 ± 0.011	0.91 ± 0.059
Merapi	M-HA-1 4B-7	2266	0.155	1.04 ± 0.013	0.52 ± 0.022	0.88 ± 0.041
Merapi	M-HA-1 4B-8	2233	0.160	0.97 ± 0.079	0.54 ± 0.027	0.81 ± 0.056
Merapi	M-HA-1 4B-9	2254	0.162	0.97 ± 0.008	0.66 ± 0.210	0.73 ± 0.227
Merapi	M-HA-1 4B-10	2189	0.182	0.94 ± 0.004	0.43 ± 0.001	0.99 ± 0.003
Merapi	M-HA-2* 3B-4	2061	0.215	0.78 ± 0.076	0.60 ± 0.094	0.66 ± 0.185
Merapi	M-HA-2* 3B-5	2013	0.233	0.80 ± 0.037	0.51 ± 0.087	0.79 ± 0.103
Merapi	M-HA-2* 3B-6	2036	0.220	0.86 ± 0.066	0.51 ± 0.043	0.82 ± 0.019
Merapi	M-HA-2* 3B-7	2108	0.188	0.86 ± 0.060	0.50 ± 0.027	0.83 ± 0.021
Merapi	M-HA-2* 3B-8	2173	0.163	0.88 ± 0.008	0.55 ± 0.045	0.75 ± 0.063
Merapi	M-HA-2* 3B-9	1990	0.242	0.79 ± 0.049	0.46 ± 0.004	0.86 ± 0.046
Merapi	M-HA-2* 3B-10	1938	0.263	0.79 ± 0.011	0.47 ± 0.042	0.88 ± 0.067
Merapi	M-HA-2* 3B-11	2166	0.168	0.85 ± 0.028	0.45 ± 0.093	0.93 ± 0.195
Merapi	M-SA-1 1A-4	2116	0.231	0.75 ± 0.061	0.45 ± 0.062	0.80 ± 0.107
Merapi	M-SA-1 1A-6	2102	0.236	0.76 ± 0.052	0.51 ± 0.018	0.70 ± 0.071
Merapi	M-SA-1 1A-8	2033	0.262	0.76 ± 0.038	0.55 ± 0.105	0.70 ± 0.109

Merapi	M-SA-1 1A-10	2048	0.256	0.75 ± 0.049	0.47 ± 0.052	0.78 ± 0.062

996

997 **Table 3**. Average connected porosity, bulk sample density (of the water-saturated
998 samples), thermal conductivity, thermal diffusivity, and specific heat capacity for the
999 water-saturated andesites from Mt. Ruapehu. Asterisk indicates that the sample
1000 contains cristobalite (see Heap and Kennedy, 2016). Quoted values of thermal
1001 conductivity and thermal diffusivity are the average of four measurements. The
1002 specific heat capacity was calculated by dividing the specific heat per unit volume,
1003 given by the Hot Disk device (using the average of the four measurements), by the
1004 bulk sample density. The standard deviations provided relate to measurement
1005 precision (calculated using the four measurements). The standard uncertainty for
1006 values of thermal conductivity and thermal diffusivity using the transient hot-strip
1007 method has been determined to be 2.6 and 11%, respectively (Hammerschmidt and
1008 Sabuga, 2000).
1009

Volcano	Sample number	Average bulk sample density, ρ_b (kg.m^{-3})	Average connected porosity	Thermal conductivity, λ (W.m^{-1}.K^{-1})	Thermal diffusivity, D (mm^2.s^{-1})	Specific heat capacity, C_p (kJ.kg^{-1}.K^{-1})
Ruapehu	R1*	2765	0.030	1.95 ± 0.068	0.85 ± 0.113	0.84 ± 0.107
Ruapehu	R2*	2730	0.030	1.67 ± 0.021	0.75 ± 0.027	0.82 ± 0.029
Ruapehu	R3*	2744	0.044	1.92 ± 0.046	0.78 ± 0.094	0.90 ± 0.091
Ruapehu	R4*	2712	0.037	1.67 ± 0.021	0.75 ± 0.027	0.83 ± 0.029
Ruapehu	R5	2732	0.026	1.52 ± 0.056	0.63 ± 0.032	0.88 ± 0.027
Ruapehu	R6	2694	0.045	1.51 ± 0.063	0.64 ± 0.062	0.88 ± 0.051
Ruapehu	R7	2438	0.195	1.37 ± 0.030	0.54 ± 0.045	1.04 ± 0.066
Ruapehu	R8	2586	0.108	1.47 ± 0.021	0.60 ± 0.061	0.96 ± 0.105
Ruapehu	R9	2522	0.147	1.42 ± 0.042	0.57 ± 0.053	0.99 ± 0.074
Ruapehu	R10	2505	0.158	1.42 ± 0.034	0.60 ± 0.033	0.96 ± 0.049

Ruapehu	R11	2530	0.140	1.42 ± 0.040	0.61 ± 0.012	0.92 ± 0.021
Ruapehu	R12	2440	0.193	1.35 ± 0.024	0.55 ± 0.008	1.01 ± 0.020
Ruapehu	R14	2192	0.333	1.27 ± 0.025	0.49 ± 0.023	1.20 ± 0.080
Ruapehu	R15	2182	0.341	1.31 ± 0.061	-	-
Ruapehu	R17	1649	0.615	0.90 ± 0.024	0.27 ± 0.010	2.02 ± 0.021

1010

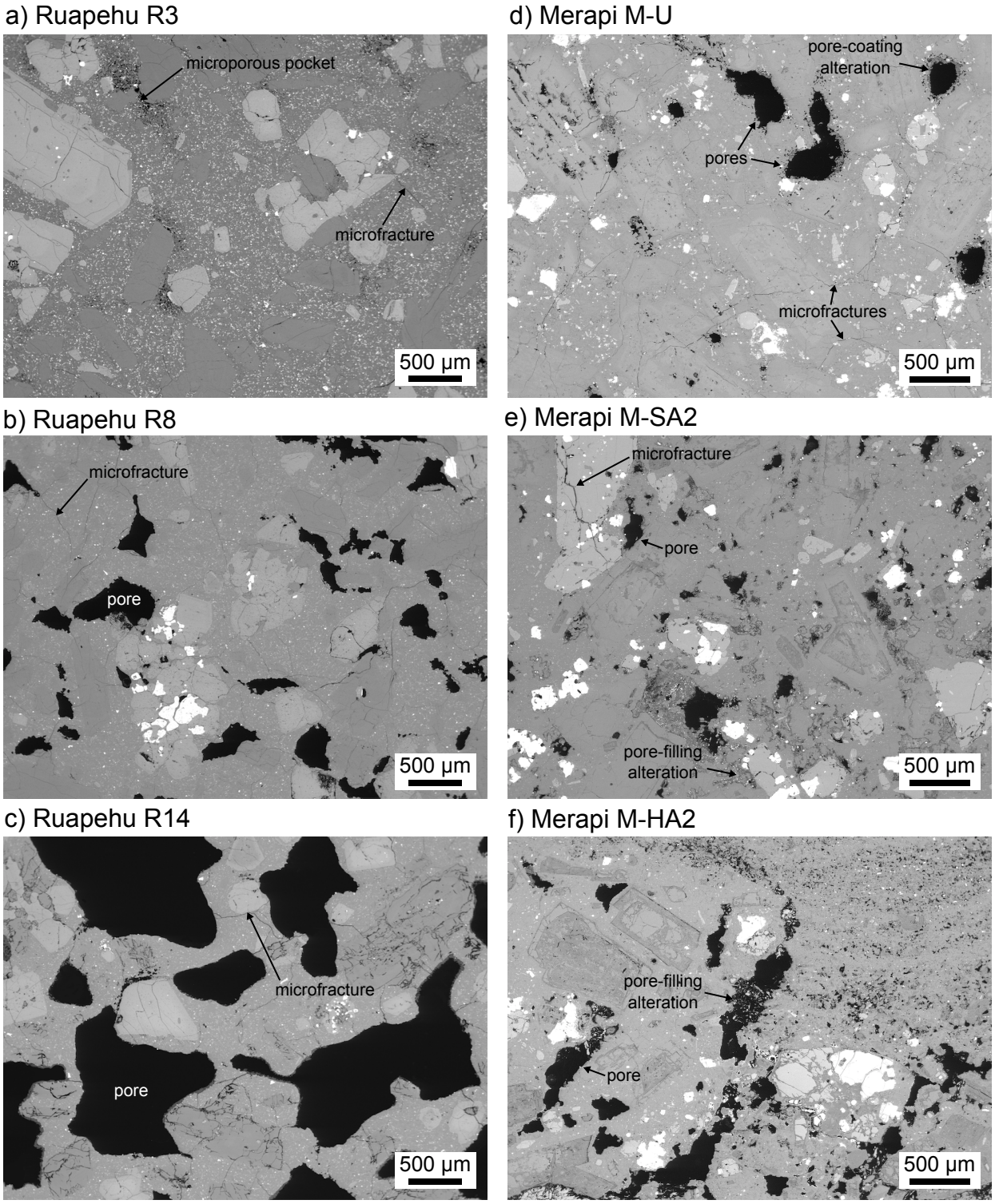

Figure 1; Heap et al., JVGR

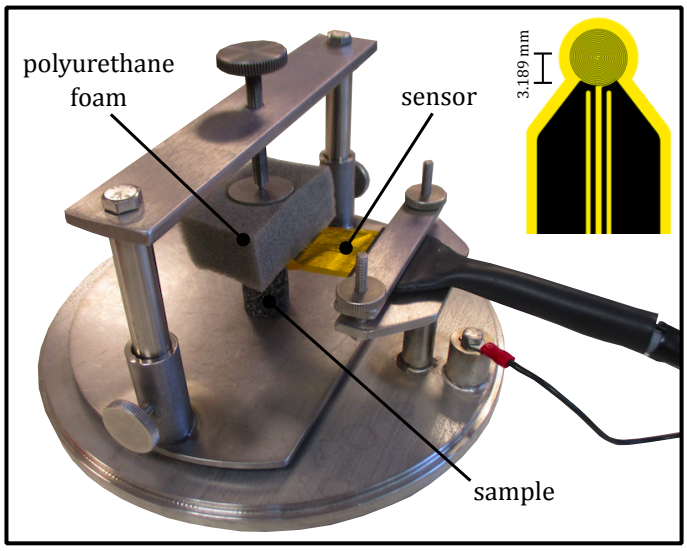

Figure 2; Heap et al., JVGR

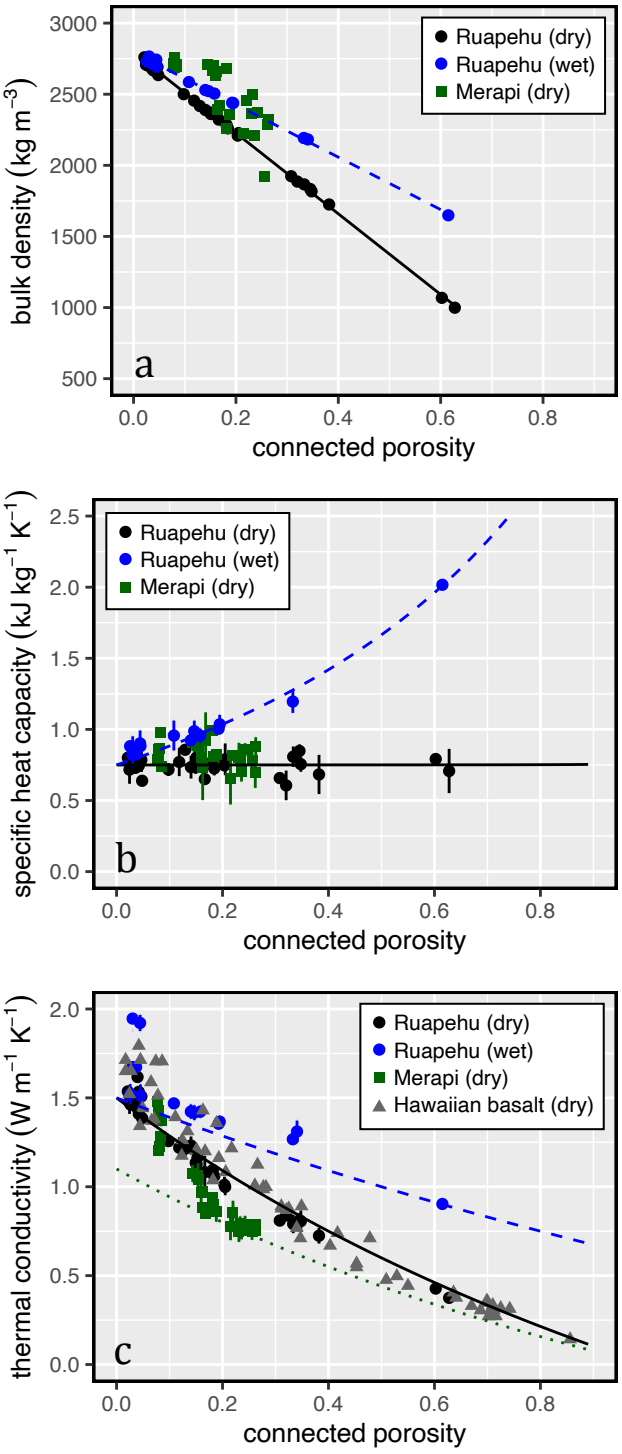

Figure 3; Heap et al., JVGR

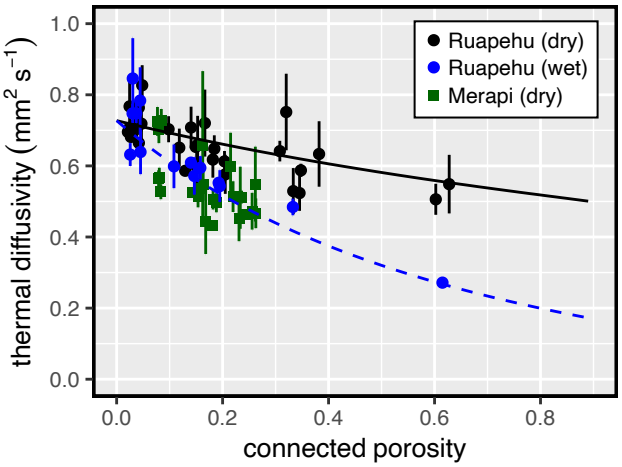

Figure 4; Heap et al., JVGR

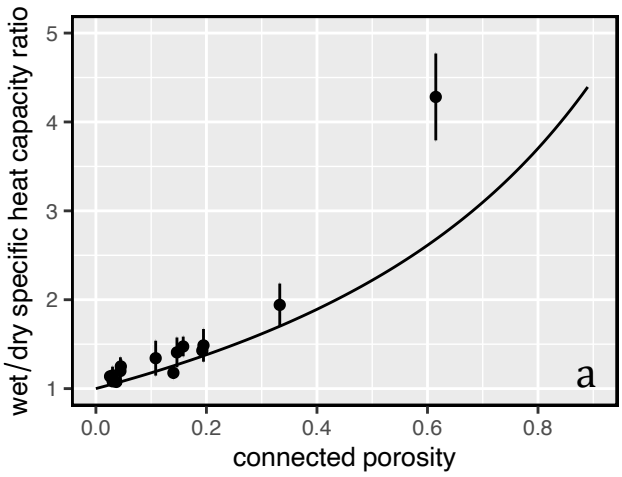

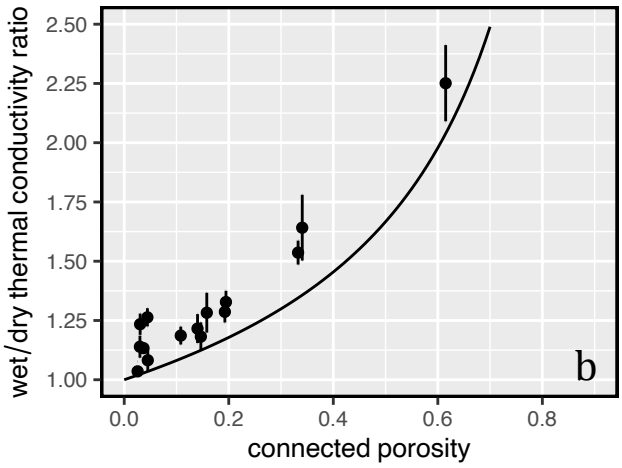

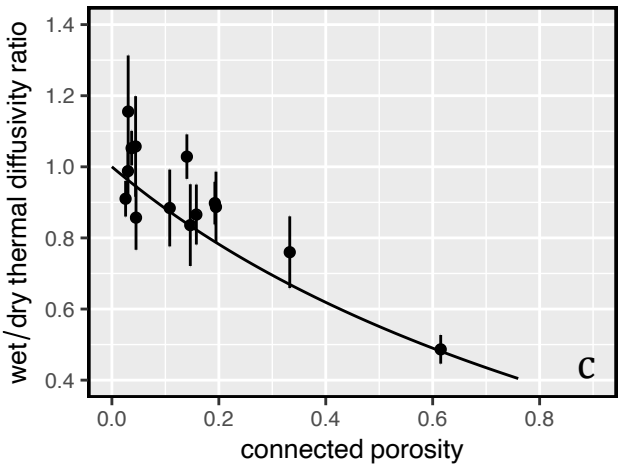

Figure 5; Heap et al., JVGR

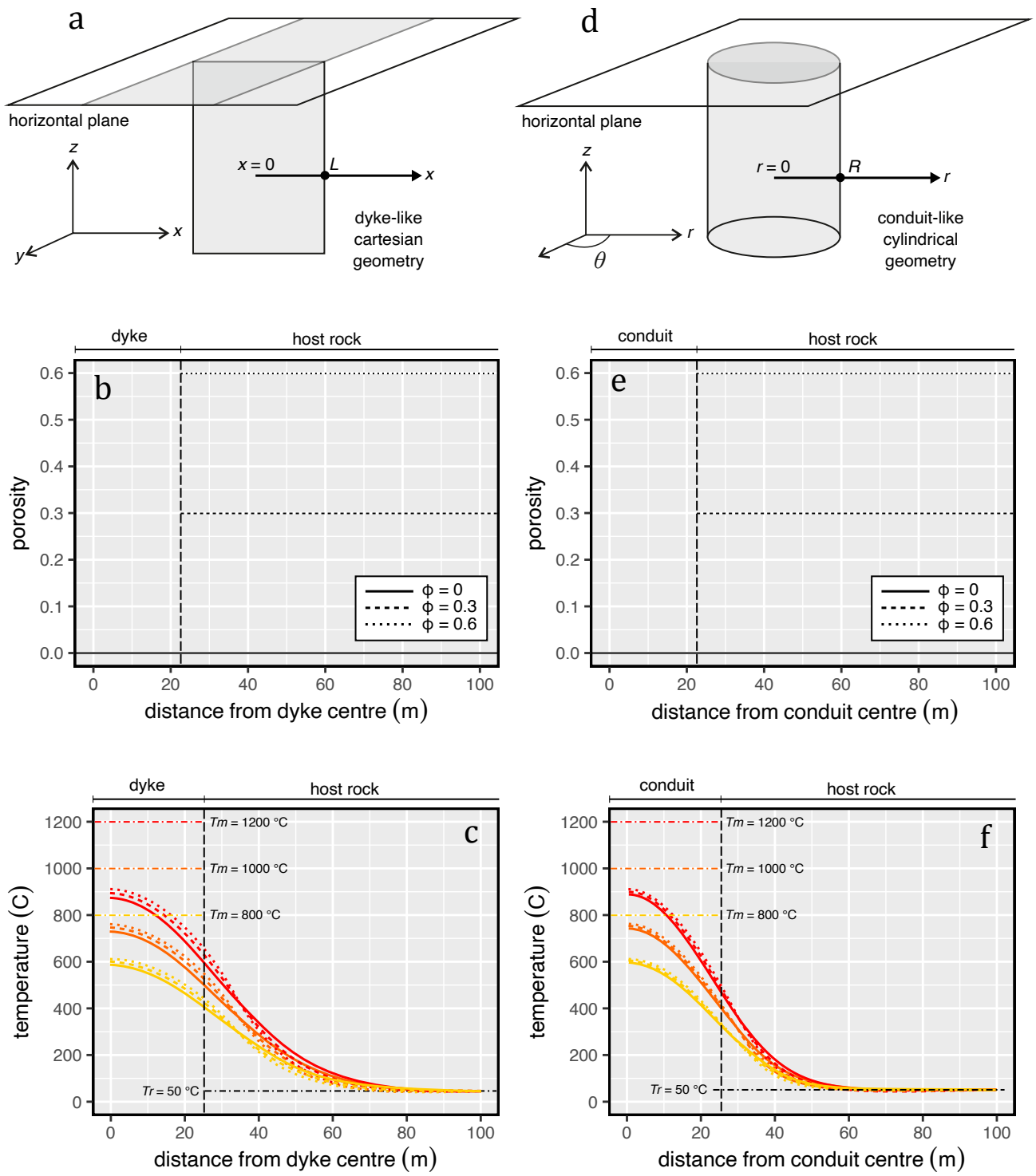

Figure 6; Heap et al., JVGR

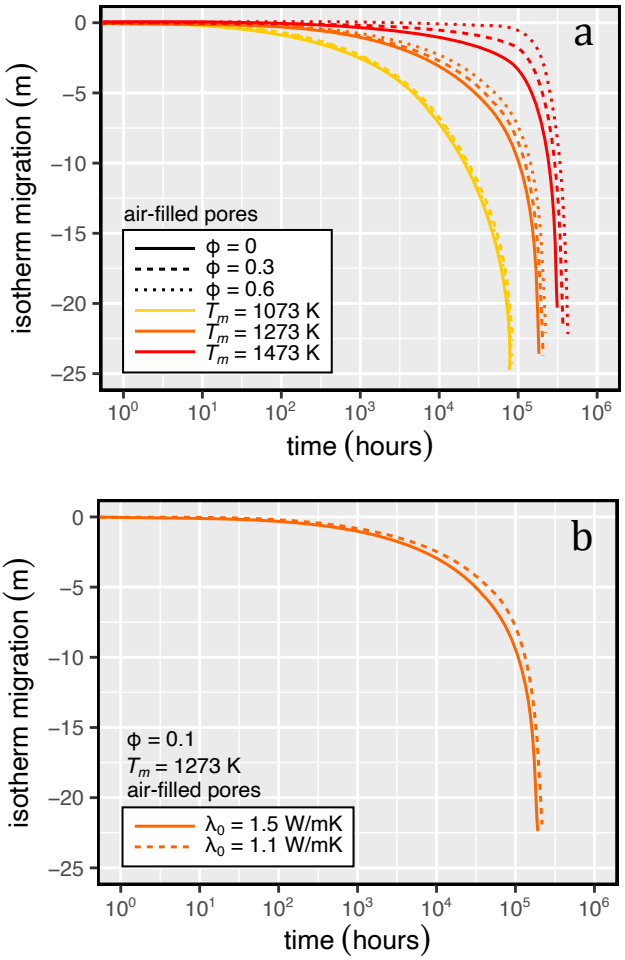

Figure 7; Heap et al., JVGR

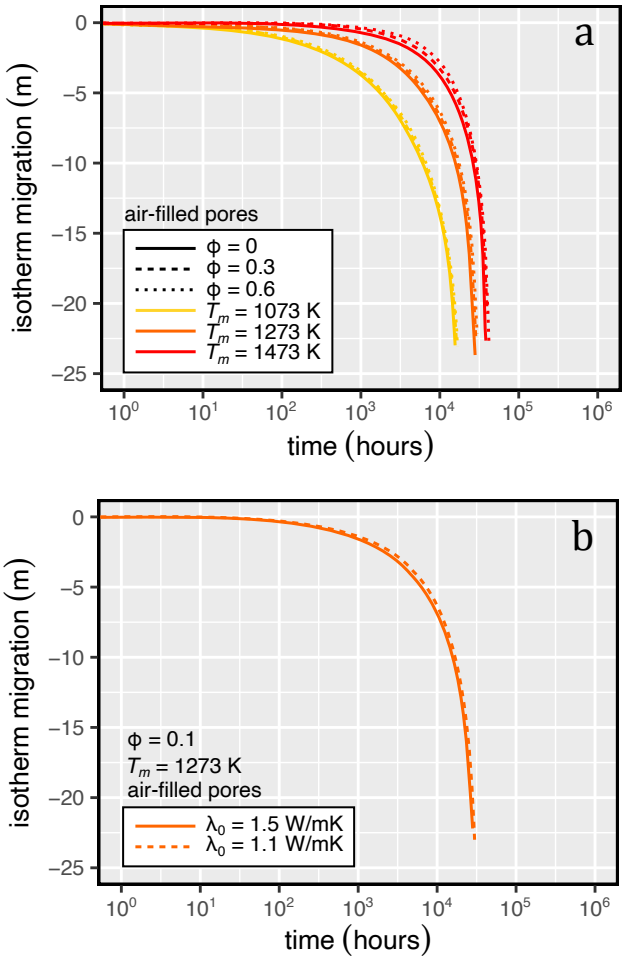

Figure 8; Heap et al., JVGR

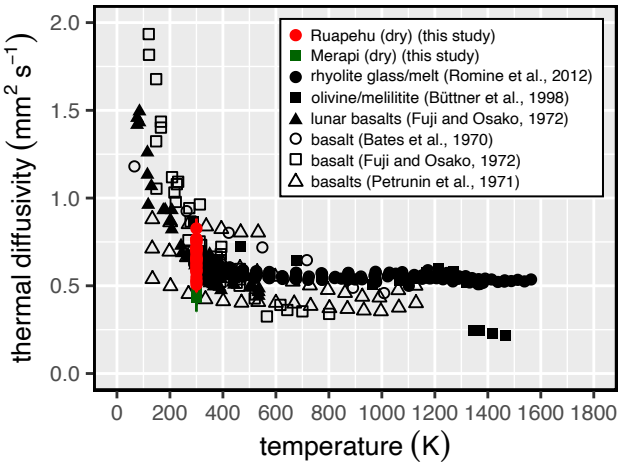

Figure 9; Heap et al., JVGR